PCCP

Cite this: *Phys. Chem. Chem. Phys.*, 2012, **14**, 14460–14485

www.rsc.org/pccp

PERSPECTIVE

Optimal control theory – closing the gap between theory and experiment

Philipp von den Hoff, Sebastian Thallmair, Markus Kowalewski, Robert Siemering and Regina de Vivie-Riedle*

Received 1st June 2012, Accepted 8th August 2012
DOI: 10.1039/c2cp41838j

Optimal control theory and optimal control experiments are state of the art tools to control quantum systems. Both methods have been demonstrated successfully for numerous applications in molecular physics, chemistry and biology. Modulated light pulses could be realized, driving these various control processes. Next to the control efficiency, a key issue is the understanding of the control mechanism. An obvious way is to seek support from theory. However, the underlying search strategies in theory and experiment towards the optimal laser field differ. While the optimal control theory operates in the time domain, optimal control experiments optimize the laser fields in the frequency domain. This also implies that both search procedures experience a different bias and follow different pathways on the search landscape. In this perspective we review our recent developments in optimal control theory and their applications. Especially, we focus on approaches, which close the gap between theory and experiment. To this extent we followed two ways. One uses sophisticated optimization algorithms, which enhance the capabilities of optimal control experiments. The other is to extend and modify the optimal control theory formalism in order to mimic the experimental conditions.

1 Introduction

A generally defined goal in chemistry is the controlled and quantitative conversion of the given reagent into a desired product. Traditionally this is achieved by adjusting the thermo dynamics of the reaction through the external parameters temperature, pressure, concentration and solvent. An alternative route is the manipulation of the reaction kinetics by adding appropriate catalysts.

Department of Chemistry, Ludwig Maximilians Universität München, Butenandtstr. 11, 81377 München, Germany.
E mail: Regina.de_vivie@cup.uni muenchen.de

The first experimental realization of a laser in the sixties added a new dimension to the capabilities for controlling reactions, as these special light sources now offer the oppor tunity to control quantum systems coherently. Along this line several ideas were developed to utilize this new control tool. The first theoretical proposals discussed three different approaches using single parameter control in the 1980s. In the Brumer Shapiro control scheme, the interference between different light induced reaction pathways is used for the control.[1,2] The stimulated Raman adiabatic passage (STIRAP) uses two suitably timed laser interactions to achieve complete population transfer in three state Λ type quantum systems.[3,4]

Philipp von den Hoff

Philipp von den Hoff was born in Munich, Germany. He received the Diploma degree in chemistry from the Ludwig Maximilians University of Munich in 2007 and obtained his PhD in theoretical chemistry there in 2012. During his Diploma and PhD thesis, he performed theoretical studies on coupled electron and nuclear dynamics in small molecules and their coherent control.

Sebastian Thallmair

Sebastian Thallmair was born in Munich, Germany. He received the Master of Science in chemistry from the Ludwig Maximilians University, Munich, in 2010. During his Master degree and ongoing PhD studies, he has been working in theory and in experiment on ultrafast molecular processes ranging from the femtosecond to the nanosecond regime.

In the Tannor Kosloff Rice pump dump scheme, laser light is used to create and steer nuclear wavepackets to control a molecular reaction.[5,6] The first experimental realization was demonstrated by Zewail and coworkers.[7,8] Extension of this concept to multi parameter control[9,10] has come within reach due the development of femtosecond laser pulses in combi nation with elaborate pulse shaping techniques.[11]

Up to now this concept of coherent control was successfully realized within several molecular reactions in closed loop experiments.[12–15] In these experiments the yield of a predefined reaction product was optimized by tailoring the driving laser field in a pulse shaping device. Liquid crystal optical modu lators, often used in the control experiments, work in the frequency domain and are able to control the laser parameters amplitude, phase and nowadays also the polarization.[16–18] The optimal laser pulse for the desired task is found by using sophisticated search algorithms, in most cases genetic algo rithms. The resulting optimized electric fields are often very complex, thus it is nearly impossible to understand the underlying processes involved in the observed control. To reduce the complexity of the shaped laser fields in optimal control experiments (OCE), the experimentalists started to use analytic, parameterized phase functions such as sinusoidal phase modulation to control a quantum system.[19–27] But this reduction of the search space does not lead to sufficient understanding of the mechanisms that steer a reaction.

From the theory side, optimal pulses steering a reaction coherently from the given reagent to a predefined product can be found in a more direct way by utilizing for instance the powerful approach of optimal control theory (OCT).[5,28–33] In general, this method works in the time domain and uses the known Hamiltonian of the quantum system to iteratively calculate the electromagnetic field, which drives the system most efficiently from a given initial state to the desired target state. In this perspective we concentrate on the full quantum mechanical treatment. For a comprehensive review on semi classical control see ref. 34.

With this theory in hand, there was the hope that now the fundamental processes leading to coherent control could be identified by bringing the OCT in close contact to the OCE. But the basic implementation of this theory exhibits no constraints or requirements on the optimized electric fields. Consequently, the theoretically achieved results could not be compared to the OCE, as the emerging fields were often much too complex and could not be implemented in an experimental setup. In fact, there were many experimental limitations that made it impossible to compare the OCT results to the results of the OCE. The experimental restrictions especially show up in the pulse shape, in the pulse bandwidth, in the central frequency of the pulse and in the frequency resolution of the spatial light modulator *e.g.* the number of pixels used in the shaping device.[35]

In terms of the pulse shape one has to ensure in the theoretical description a smooth build up and attenuation of the electric field, in order to realize the calculated optimal electric fields in experiments. Moreover, the interplay between the bandwidth of the pulse and the experimentally available pixels in the pulse shaper determines the number of control knobs.

Markus Kowalewski

Markus Kowalewski was born in Dachau, Germany. He received the master's degree in chemistry from the Ludwig Maximilians University (LMU), Munich, in 2007. During the master's and PhD degrees, he was working in the field of cold molecules, their quantum dynamical treatment and on optimal control theory. In 2012 he finished his PhD thesis in theoretical chemistry at the LMU. He has now a postdoc position at the centre of interdisciplinary mathe matics of the University of Uppsala. His main research interests are the quantum dynamical description of molecules and their applications to chemical problems.

Robert Siemering

Robert Siemering was born in Munich, Germany. He received the Master of Science in chemistry from Ludwig Maximilians University, Munich, in 2011. During his Master thesis and ongoing PhD work, he has been performing theoretical studies on the selective population of dressed states and on coupled electron and nuclear dynamics in small molecules.

Regina de Vivie-Riedle

Regina de Vivie Riedle was born in Wuppertal, Germany. She graduated in chemistry from the Friedrich Wilhelm University of Bonn, Germany, in 1987. In 1997, she did the Habilitation in Theoretical Chemistry at the Freie University Berlin. She did two Postdocs, one at the MPI for Quantum Optics (MPQ) in Garching and one at the Joint Institute for Laboratory Astro physics (JILA) in Boulder. From 1997 to 2002 she was a C3 professor at the MPQ. Since 2003, she has been the leader of the theoretical femto science group at the Ludwig Maximilians University in Munich. Her research topics are ultrafast photoinduced molecular dynamics and coherent control theory.

This number also has to be adjusted in the theory, as here it is usually much larger and only related to the number of time steps used in the calculation. In addition, one has to take into account that the spatial light modulator only controls the amplitude, phase and sometimes the polarization of the incident pulse, but not or only to a small extent its central frequency. In the general implementation of OCT, this parameter is also completely unrestricted and thus also leads to a mismatch between OCT and OCE. This mismatch is even enlarged when the search space is reduced to physically motivated parameters for the benefit of interpretable light fields.

To bring theory and experiment in closer contact, one needs to extend the OCT in order to mimic the real experimental conditions. In this perspective we review some modifications of the OCT accompanied with corresponding results of our recent work that close the gap between OCT and OCE. In addition we also review theoretical approaches working in the frequency domain, which can be implemented directly in the respective experiments. The selected examples are isolated molecules as we focus on the inherent properties of the system. For insufficient protected systems the interaction with the environment has to be included. Suitable solutions in the wavepacket formalism have been proposed by Kosloff and coworkers.[36] A general limit of tolerable decoherence during control has been pointed out by Rabitz *et al.*, showing that it is not possible to achieve high yields if the coherence lifetime is short compared to the control interaction time.[37]

The article is organized as follows: first, we give a brief introduction into the theoretical framework of OCT formalism, especially with regard to the extensions to mimic the inherent experimental conditions. Subsequently we discuss several examples where we used OCT to optimize either electronic (Section 3) or vibrational transitions (Section 4) in molecules.

2 Optimal control theory

In the following section the basic formalism of OCT will be introduced. Based on the presented fundamental ideas of this theory, we subsequently discuss various extensions of OCT, which we used and demonstrated in the following examples. In this sense, we especially show, how we introduced frequency constraints.

2.1 Multi-target optimal control theory

Here, an optimality criterion has to be achieved and the method finds an appropriate control law for it, the optimal laser field. Different OCT concepts for quantum control investigations were developed, predominantly in the groups of H. Rabitz,[30,31] D. Tannor and S. Rice,[5,32] based on the calculus of variations. In general, the following OCT functional (eqn (1)) has to be maximized.

$$J(\psi_i(t),\psi_f(t),\varepsilon(t)) = F(\tau) \int_0^T \alpha(t)|\varepsilon(t)|^2 dt \int_0^T \psi_f(t)\, G(\psi_i(t),\varepsilon(t))dt \quad (1)$$

It includes three terms, the optimization aim $F(\tau)$, an integral over the laser field, penalizing the pulse fluence and an ancillary constraint. In the most general case, the optimization aim $F(\tau)$ is to transfer an initial state wavefunction ψ_i into a final state ϕ_f after the laser excitation time T. In a more general fashion, the algorithm is asked to fulfill several transitions starting form various initial states to predefined target states with the same laser pulse. This formulation is known as multi target optimal control theory (MTOCT)[38] and it serves as a basis throughout this section. The definition of $F(\tau)$ is formulated as the sum over the absolute squares of the scalar products between the initial states $\psi_{ik}(T)$, propagated in time with the target states ϕ_{fk}:

$$F(\tau) = \sum_{k\ 1}^{N} |\langle\psi_{ik}(T)|\phi_{fk}\rangle|^2. \quad (2)$$

The second term of eqn (1) is an integral over the laser field $\varepsilon(t)$ with a time dependent factor $\alpha(t)$. In principle, high values of α assure low field intensities and complexities. Depending on the implementation, it is known as the penalty factor or Krotov change parameter. With the choice of $\alpha(t)$ $\alpha_0/s(t)$ and *e.g.* a sinusoidal shape function $s(t)$, an envelope function can be impressed on the laser field.[33,39] This guarantees smooth switching on and off behavior of the pulse, instead of abrupt field intensity changes for the times t $0,T$, which is crucial for the implementation of such optimized pulses in the experiment.

The last term of the functional (eqn (1)) comprises the time dependent Schrödinger equation as an ancillary constraint, denoted by $G(\psi_i(t), \varepsilon(t))$, with the Lagrange multiplier $\psi_f(t)$:

$$\int_0^T \psi_f(t)G(\psi_i(t),\varepsilon(t))dt = 2\Re[C\int_0^T \langle\psi_f(t)|i[\hat{H}_0 \quad \hat{\mu}\varepsilon(t)] + \frac{\partial}{\partial t}|\psi_i(t)\rangle dt]. \quad (3)$$

Separable differential equations can be derived from this form due to the formulation $2\Re$ in eqn (3) and a suitable choice of the factor C in dependence on the definition of the optimization aim. For multi target optimal control theory (MTOCT) the factor C in the ancillary constraint includes a sum, running over all k transitions. The complete multi target functional reads:

$$J(\psi_{ik}(t),\psi_{fk}(t),\varepsilon(t)) = \sum_{k\ 1}^{N}\left\{|\langle\psi_{ik}(T)|\phi_{fk}\rangle|^2 2\Re\left[\langle\psi_{ik}(T)|\phi_{fk}\rangle\int_0^T \langle\psi_{fk}(t)|i[\hat{H}_0 \quad \hat{\mu}\varepsilon(t)] + \frac{\partial}{\partial t}|\psi_{ik}(t)\rangle dt\right]\right\} \alpha_0\int_0^T \frac{|\varepsilon(t)|^2}{s(t)}dt. \quad (4)$$

The calculation of optimal laser fields now relies on finding the extreme of the functional $J(\psi_{ik}(t), \psi_{fk}(t), \varepsilon(t))$ (eqn (4)) with respect to the functions $\psi_{ik}(t)$, $\psi_{fk}(t)$ and $\varepsilon(t)$. The derivative of the functional with respect to $\psi_{fk}(t)$ and $\psi_{ik}(t)$ leads to the following coupled equations of motion:

$$i\frac{\partial}{\partial t}\psi_{ik}(t) = [\hat{H}_0 \quad \hat{\mu}\varepsilon(t)]\psi_{ik}(t),\ \psi_{ik}(0) = \phi_{ik}, \quad (5)$$

$$i\frac{\partial}{\partial t}\psi_{fk}(t) = [\hat{H}_0 \quad \hat{\mu}\varepsilon(t)]\psi_{fk}(t),\ \psi_{fk}(T) = \phi_{fk}, \quad (6)$$

with the corresponding boundary conditions. The propagated wavefunctions $\psi_{ik}(t)$ have to correspond to the initial states ϕ_{ik} at the time t 0 and the Lagrange multipliers are equal to the target states at the end of the propagation $\psi_{fk}(T)$ ϕ_{fk}. According to Zhu and Rabitz,[31] the functional (eqn (4)) is also differentiated with respect to the laser field $\varepsilon(t)$, where only linear terms are kept and terms containing $(\delta\varepsilon(t))^2$ are neglected.

$$\begin{aligned}\delta_{\varepsilon(t)}J = {} & J(\psi_{ik}(t),\psi_{fk}(t),\varepsilon(t)+\delta\varepsilon(t)) \quad J(\psi_{ik}(t),\psi_{fk}(t),\varepsilon(t)) \\ \approx {} & \sum_{k\ 1}^{N}\int_0^T\left[2\alpha_0\frac{\varepsilon(t)}{s(t)}\right. \\ & \left. + 2J\langle\psi_{ik}(T)|\phi_{fk}\rangle\langle\psi_{fk}(t)|\hat{\mu}|\psi_{ik}(t)\rangle\right]\delta\varepsilon(t)\mathrm{d}t = 0\end{aligned} \tag{7}$$

Under the consideration that the time evolution of the wave function is unitary, one obtains the relationship

$$\langle\psi_{ik}(T)|\phi_{fk}\rangle \quad \langle\psi_{ik}(t)|\psi_{fk}(t)\rangle. \tag{8}$$

Since there is no incident condition imposed on $\delta\varepsilon(t)$, eqn (7) is fulfilled when the integrand turns zero. Using eqn (8) a formula constructing the improved electric field $\varepsilon^{j+1}(t)$ can be derived.

$$\varepsilon^{j+1}(t) = \frac{s(t)}{\alpha_0 N}\Im\left[\sum_{k\ 1}^{N}\langle\psi_{ik}(t)|\psi_{fk}(t)\rangle\langle\psi_{fk}(t)|\hat{\mu}|\psi_{ik}(t)\rangle\right]. \tag{9}$$

The coupled eqn (5), (6) and (9) can be interpreted in different ways, and different methods to obtain the optimal field were proposed. The schemes can be based on gradient type optimization of the laser fields.[40,41] Alternatively, the Krotov method, which is a global iterative procedure, was developed.[32,42,43] In this case, the $2N + 1$ coupled differential equations (eqn (5), (6) and (9)) are solved iteratively in a self consistent way, which proceeds as follows: The target states $\psi_{fk}(T)$ are propagated backward in time with the electric field of the current iteration $\varepsilon^j(t)$ (eqn (6)). Afterwards, simultaneous propagation forward in time of the initial wavefunctions $\psi_{ik}(0)$ and the target wavefunctions $\psi_{fk}(0)$ takes place (eq (5) and (6)), where the new field is determined in each step as intermediate feedback according to eqn (9). This field is then used in the next iteration for back propagation. Also, schemes using an immediate feedback from the control field in an entangled fashion were proposed, where quadratic convergence is reached.[44]

According to Koch *et al.*,[45] the constraint on the pulse fluence (second term in eqn (1)) can also be chosen to take the form:

$$\int_0^T\frac{\alpha_0}{s(t)}[\varepsilon(t) \quad \varepsilon'(t)]^2, \tag{10}$$

in the OCT functional (eqn (4)), where $\varepsilon'(t)$ corresponds to the electric field from the previous iteration. The constraint restricts the change in pulse energy in each iteration with the Krotov change parameter α_0. In the next iteration step of MTOCT, the improved laser field $\varepsilon^{j+1}(t)$ is constructed as follows:

$$\varepsilon^{j+1}(t) = \varepsilon^j(t) + \frac{s(t)}{\alpha_0 N}\times\Im\left[\sum_{k\ 1}^{N}\langle\psi_{ik}(t)|\psi_{fk}(t)\rangle\langle\psi_{fk}(t)|\hat{\mu}|\psi_{ik}(t)\rangle\right]. \tag{11}$$

This method is known as the modified Krotov OCT scheme.

2.2 Phase sensitive targets

In the standard OCT, the aim $F(\tau)$ is formulated as the square of the scalar product of the initial state, propagated in time with the target state. This definition allows us to control the spatial position and shape of the optimized wavefunction but not its phase. To gain control also over the phase of a wavefunction in the framework of OCT is crucial for various applications.[43,46–48] This control can be achieved by choosing

$$F(\tau) = \Re\left[\sum_{k\ 1}^{N}\langle\psi_{ik}(T)|\phi_{fk}\rangle\right] \tag{12}$$

as the optimization aim. To derive separable differential equations, the factor C in eqn (3) is assigned to C 1. The derivative of the whole phase sensitive functional with respect to $\psi_{fk}(t)$ and $\psi_{ik}(t)$ leads to the same coupled equations of motion as in eqn (5) and (6). The effect of the phase sensitive definition of the optimization aim becomes only visible in the construction of the improved laser field:

$$\varepsilon^{j+1}(t) = \frac{s(t)}{\alpha_0 N}\Im\left[\sum_{k\ 1}^{N}\langle\psi_{fk}(t)|\hat{\mu}|\psi_{ik}(t)\rangle\right]. \tag{13}$$

By implementing this equation in the Krotov global iterative procedure (see Section 2.1), control over the spatial position and shape and the absolute phase of the optimized wave function is achieved. As a slight drawback, this solution allows large changes of the electric field from one iteration step j to the next step $(j + 1)$, which is especially important if the initial guess does not resemble the optimal field. But on the other hand, this OCT modification includes a very strict target definition and so the algorithm does not converge very fast.

2.3 Projection operator targets

For several control applications target wavefunctions as control aim are not appropriate. Instead, quantum control over the expectation value of a positive definite operator $\hat{O}$ is desired. These operations can for instance provide an easy link to experimental observables. For this purpose the control aim $F(\tau)$ can be defined as:[31,49]

$$F(\tau) = \sum_{k\ 1}^{N}\langle\psi_{ik}(T)|\hat{O}|\psi_{ik}(T)\rangle. \tag{14}$$

To derive again separable differential equations, the factor C in eqn (3) is assigned to C 1. The derivative of $J(\psi_{ik}(t), \psi_{fk}(t), \varepsilon(t))$ with respect to $\psi_{fk}(t)$ and $\psi_{ik}(t)$ also leads to equations of motion similar to those in eqn (5) and (6). As no final wavefunction is defined in this case, the boundary condition in eqn (6) changes to

$$\phi_{fk} = \psi_{fk}(T) = \frac{\hat{O}\psi_{ik}(T)}{||\hat{O}\psi_{ik}(T)||^2}. \tag{15}$$

The functional J is also differentiated with respect to the laser field $\varepsilon(t)$. Following the steps described in Section 2.1 and utilizing the relation in eqn (15) one can calculate the laser field:

$$\varepsilon^{j+1}(t) = \frac{s(t)}{\alpha_0 N}\Im\left[\sum_{k\ 1}^{N}\langle\psi_{fk}(t)|\hat{\mu}|\psi_{ik}(t)\rangle\right]. \tag{16}$$

Now, the $2N + 1$ coupled differential equations (eqn (5), (6) and (16)) are solved iteratively in the following way: the initial states $\psi_{ik}(t)$ are propagated forward in time with the electric field $\varepsilon^j(t)$ (*i.e.* solve the time dependent Schrödinger eqn (5)). Then the targets ϕ_{fk} are constructed by application of the operator $\hat{O}$ to $\psi_{ik}(T)$. Afterwards, the wavefunctions $\psi_{ik}(t)$ and $\psi_{fk}(t)$ are used to construct an improved field $\varepsilon^{j+1}(t)$ by simultaneously propagating $\psi_{ik}(t)$ and $\psi_{fk}(t)$ backward in time from $t = T$ to $t = 0$ with the field $\varepsilon^j(t)$. In each time step the optimized field $\varepsilon^{j+1}(t)$ is determined by using eqn (16). This field is then used in the next iteration for forward propagation and the construction of the target.

2.4 Constraints in the frequency domain

In the basic formalisms, OCT has no constraints with respect to the frequency domain. Thus the algorithm can vary the spectrum freely to find the optimal solution. In contrast, the OCE completely works in the frequency domain and thereby restricts the central frequency in a very defined way. In addition, some applications like non resonant multi photon processes need explicit constraints in the frequency domain within the OCT formalism.[50,51] To achieve this goal, a modified implementation of OCT based on the Krotov method, which allows for strict limitations on the spectrum, was developed and will be reviewed here. The new multi target optimal control functional which adds constraints in the frequency domain takes the form

$$\begin{aligned} &K[\psi_{fk}(t),\psi_{ik}(t),\gamma(t),\varepsilon(t)] \\ &= \sum_{k=1}^{N}\Big\{|\langle\psi_{ik}(T)|\phi_{fk}\rangle|^2 \\ &\quad \alpha_0\int_0^T \frac{|\varepsilon(t) - \varepsilon'(t)|^2}{s(t)}\mathrm{d}t \quad \gamma(t)\int_0^T |G(\varepsilon(t))| \\ &\quad 2\Re\left[\langle\psi_{ik}(T)|\phi_{fk}\rangle\int_0^T\langle\psi_{fk}(t)|\left[i(\hat{H}_0 - \hat{\mu}\varepsilon(t)) + \frac{\partial}{\partial t}\right]|\psi_{ik}(t)\rangle\mathrm{d}t\right]\Big\}. \end{aligned} \tag{17}$$

A new frequency constraint is introduced in the MTOCT functional (eqn (17)), by an additional side condition

$$S = \gamma(t)\int_0^T |G(\varepsilon(t))| = 0, \tag{18}$$

where the transformation $G(\varepsilon(t))$ acts as a frequency filter on the electric field. The corresponding Lagrange multiplier is $\gamma(t)$. If G is chosen to remove all components from the spectrum representing a valid solution, the side condition $S = 0$ is fulfilled. The filter operation is formulated in the time domain and thus can be treated with a FIR filter,[52] which can be regarded as a convolution with a frequency mask:

$$G(\varepsilon(t)) = \sum_{i=0}^{M} c_i\varepsilon(t - i\Delta t), \tag{19}$$

where c_i are the FIR filter coefficients and Δt is the step size in the discrete time representation. It becomes clear from eqn (18) and (19) that the side condition is only linearly dependent on $\varepsilon(t)$. The functional derivative with respect to the electric field yields the Lagrange multiplier $\gamma(t)$:

$$\frac{\delta S[\varepsilon(t)]}{\delta\varepsilon(t)} = \gamma(t). \tag{20}$$

If the complete functional derivative with respect to $\varepsilon(t)$,

$$\frac{\delta K[\psi_{fk}(t),\psi_{ik}(t),\gamma(t),\varepsilon(t)]}{\delta\varepsilon(t)} = 0, \tag{21}$$

is solved, the expression for the electric field from eqn (11) is extended by $\gamma(t)$:

$$\begin{aligned} \varepsilon^{j+1}(t) = \varepsilon^j(t) + \frac{s(t)}{\alpha_0 N} \\ \times\Im\left[\sum_{k=1}^{N}\langle\psi_{ik}(t,\varepsilon^j)|\psi_{fk}(t,\varepsilon^{j+1})\rangle\right. \\ \left.\times\langle\psi_{fk}(t,\varepsilon^j)|\hat{\mu}|\psi_{ik}(t,\varepsilon^{j+1})\rangle\right] \quad \gamma(t). \end{aligned} \tag{22}$$

with $\varepsilon^j(t) = \varepsilon'(t)$. The Lagrange multiplier $\gamma(t)$ can be interpreted as a correction field, which substracts the undesired frequency components in each iteration. Since no additional equation has been introduced, $\gamma(t)$ cannot be determined in a direct fashion. Instead, an educated guess from the correlation between the initial and the target state is generated:

$$\gamma'(t) = \Im\left[\sum_{k=0}^{N}\langle\psi_{fk}(t,\varepsilon^j)|\psi_{ik}(t,\varepsilon^j)\rangle\times\langle\psi_{fk}(t,\varepsilon^j)|\hat{\mu}|\psi_{ik}(t,\varepsilon^j)\rangle\right]. \tag{23}$$

By removing the allowed frequencies from γ' with a simple Fourier filter, a sufficiently good guess is generated. Morever the side condition is additionally maintained by filtering the generated field after every iteration. The iterative procedure is monotonously convergent in the theoretical formulation and also in practice with approximation of the correction field.[50,51] Some other approaches using different strategies to introduce constraints in the frequency have been recently reported in ref. 53 and 54.

3 OCT to optimize transitions between electronic states in molecules

In this section we want to show how OCT can be used to optimize a reaction pathway in molecules which incorporates transitions between different electronic states. In addition, we present control strategies which modify the OCT search space in order to favor a preselected reaction path within the optimization. Therefore we review our work on the control of molecular switches (see Section 3.1) and the control realized in the SPODS scheme in the potassium dimer (see Section 3.2).

3.1 Controlling molecular switches with OCT

Fulgides are considered as promising candidates for molecular switches[55–57] that can be used as versatile devices in nano technology and for logic gates in molecular computation.

These molecules form two stable isomers, which can be swapped by a photochemical reaction (see Fig. 1). Their different absorption frequencies make them addressable individually and enable a selective read out. The active center of these molecules consists of a cyclohexadiene/all *cis* hexatriene subunit (indicated in black in Fig. 1). The opening or closure of this ring subunit is the decisive step in the switching process of the fulgides. Therefore we concentrate our investigations on the reaction of this subunit.

The ring opening of cyclohexadiene is a well known photochemical reaction following the Woodward Hoffmann rules that was studied experimentally[58–61] as well as theoretically.[62–67] After the excitation of cyclohexadiene the system evolves through various conical intersections (CoIns), leading to a branching into the ground states of both isomers cZc hexatriene and cyclohexadiene, which correspond to the isomers B and A (see Fig. 1). The following isomerization of cZc hexatriene to the more stable *trans* isomer is not important for our considerations as this reaction is sterically hindered in fulgides. The most important molecular rearrangements of this photoreaction can be described in two reactive coordinates r and φ (Fig. 1) introduced in ref. 65. The asymmetric squeezing of the ring is described by the internuclear distance r and the angle between the two indicated diagonals φ.

There are two excited electronic states involved in the reaction. It can be deduced from experiments that the initially excited electronic state is depopulated completely within 10 fs.[59] Due to this ultrashort dynamics, the coupling between the two excited states must be very strong. Therefore we merged them into one adiabatic surface.[67] The shown potential energy surfaces (Fig. 1) were derived from interpolation between

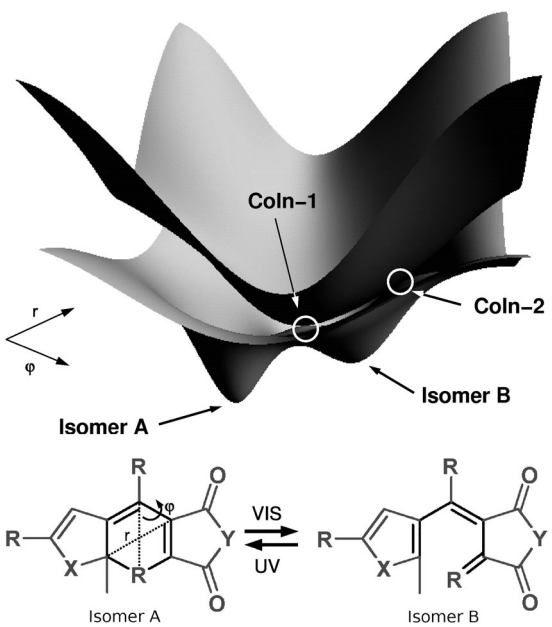

Fig. 1 The ring opening of a cyclohexadiene unit to an all cis hexatriene unit constitutes the switching process of fulgides. The reactive coordinates r and φ are indicated. The two dimensional potential energy surfaces include both minima as well as two conical intersections connecting the excited state and the ground state.

ab initio data points. The effect of the CoIns connecting the excited state with the ground state is calculated non adiabatically with the coupling elements derived by quantum chemical calculations as described in ref. 66. In the following calculations, we concentrate on the backward reaction, *i.e.* the ring closure from isomer B to isomer A. More specifically, we examine the ring opening, driven by a laser excitation in the UV/VIS regime. For an effective switch a very high quantum yield is required, thus the yield can be enhanced by the use of specially shaped femtosecond laser pulses. These pulses are optimized using OCT.

The control of reactive photochemical systems like fulgides exhibits several challenges as parts of the reaction occur in an optically dark region. This requires the generation of an excited state wavepacket with well defined shape and momentum, which subsequently evolves on the hypersurface to the target region in the ground state. In these photoreactions, where an ultrafast return to the ground state *via* CoIns is possible, vibrationally hot molecules are formed during the reaction. Their numerical treatment becomes challenging in the OCT algorithm, as forward and backward propagations are needed.[68] For the optimization of the laser induced switching by the use of the OCT algorithm, two strategies are conceivable. The first is to optimize as intermediate target a well defined wavepacket on the first excited state with respect to magnitude and direction of momentum so that it evolves through a CoIn to the desired target isomer. This solution relies on a fast transfer through the CoIn. However, this transfer is in general not completed in one step. Thus, the system has to reach the relevant CoIns several times and a loss of control is inevitable if the CoIns are located in an optically dark region as in the present case. The second strategy is to directly define a spatial part of the electronic ground state as target, which covers the desired product isomer. For our theoretical investigations we followed both routes[67,68] and the results are reviewed in Sections 3.1.1 and 3.1.2.

3.1.1 Controlling molecular switches *via* an intermediate target. To control the laser induced switching of the cyclohexadiene molecule, which is the elementary building block of the fulgides, we optimized an intermediate target on the first excited state with the help of OCT. In a previous work[69] we could already show that it is in principle possible to steer a localized wavepacket towards a conical intersection. In this case the ultimate goal is the formation of isomer A (see Fig. 1) after the relaxation through a conical intersection. The selected type of molecules holds the difficulty that initial and target state are separated in the coordinate space by an optically dark region. This entails a long period of time where the wavepacket moves without the guidance of the laser pulse. These circumstances complicate the optimization. To overcome these difficulties, we selected an intermediate target in the excited state, which is close to the Franck Condon region of isomer B.

To construct the intermediate target, the quantum dynamics with an unshaped laser pulse are analyzed and a snapshot is chosen when the wavepacket is located between the Franck Condon region and CoIn 1 (see Fig. 1). Then it is emulated by

a Gaussian wavepacket to frame the extent and the localization of the target wavepacket. The target wavepacket was provided with different momenta in r and φ. Several calculations were performed and the resulting product distributions were compared. It is important to know that the wavepackets momentum not only influences the dynamics in the excited state but also the dynamics in the ground state after the relaxation through the conical intersection. During this fully coherent process the momentum is not maintained exactly but is modified by the interaction with the non adiabatic coupling elements. From these calculations, the wavepacket that leads to the highest yield of isomer A was chosen as intermediate target. Its real part is used to construct the optimization aim (see Section 2.2) and is shown in Fig. 2(a). The nodal structure demonstrates the higher momentum in the coordinate r compared to the φ coordinate. The product ratio of this intermediate target is 94 : 6 (A : B).

In the final step the laser pulse is optimized that drives the vibrational and electronic ground state wavefunction of isomer B to this intermediate target. If the target is reached perfectly, the evolution to the ground state will be the same. As the momentum of the intermediate target plays the crucial role, we use a modification of the standard OCT algorithm, which allows for a phase sensitive optimization as discussed in Section 2.2. The real part of the wavepacket after excitation with the optimized pulse is depicted in Fig. 2(b). Comparison with the intermediate target reveals several features which both wavefunctions have in common, like the enhanced momentum along the coordinate r. The overlap between the real parts of the optimized wavefunction and intermediate target equals 0.65.

The XFROG (crossed frequency resolved optical gating) spectrum of the resulting laser pulse is shown in Fig. 3. It has a clear structure with two main frequencies and exhibits a very high excitation efficiency of more than 97%. The optimized pulse drives the wavepacket to the preselected geometry (*cf.* Fig. 2(b)) and results in a product distribution of 91 : 9 A : B in the ground state. Thus the selectivity of the intermediate target is not reached completely, but the product distribution is enhanced significantly (see Fig. 4).

To elucidate the underlying control mechanism, the time evolution of the product formation for a Gaussian laser pulse (panel a), the intermediate target (panel b) and the optimized pulse (panel c) are compared in Fig. 4. In all three dynamics the formation of isomer A occurs in two steps. While the intermediate target enlarges both steps (panel b), the optimized pulse mainly enhances the second step (panel c). Both intermediate target and optimized pulse are able to suppress the formation of isomer B. The suppress mechanism is a necessary condition to guaranty the almost flawless switching performance, achieved by the OCT algorithm.

3.1.2 Controlling molecular switches *via* a ground state target. The most straightforward control target for the switching process is the target isomer itself. This is realized by defining a spatial part of the electronic ground state, which covers the desired product (isomer A), as the target. The corresponding target operator is depicted in Fig. 5. The initial wavefunction is the vibrational ground state of isomer B.

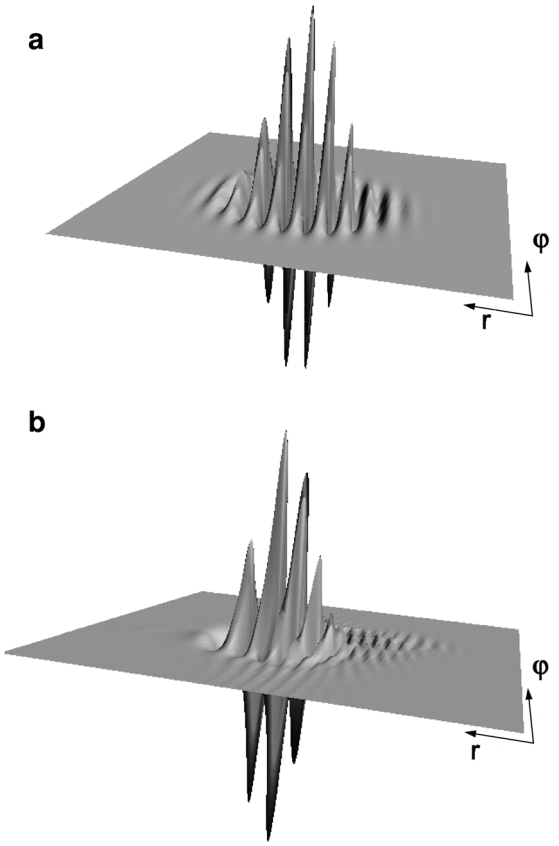

Fig. 2 Real part (a) of the intermediate target, (b) of the wavepacket after excitation with the optimized pulse.

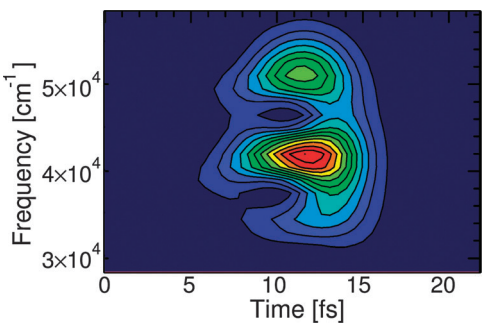

Fig. 3 XFROG spectrum of the optimized laser pulse showing two main frequency components.

Our previous calculations (Section 3.1.1) show that after the photo excitation the wavepacket leaves the Franck Condon region very fast. But this is the only region where its motion can be controlled by laser light. Subsequently it enters the dark region including the conical intersections where no further manipulation is possible. The return to the ground state takes place *via* both conical intersections CoIn 1 and CoIn 2, while the whole relaxation does not occur in one rush (*cf.* Fig. 4), but in a stepwise process. An alternative mechanism to control this reaction is an all optical process like a pump dump scheme[6] which is a fast and effective process. In addition, this process is very appropriate for the optimal control algorithm, as it is the optical process which is directly addressable by the OCT algorithm. In comparison, the conical intersections are a

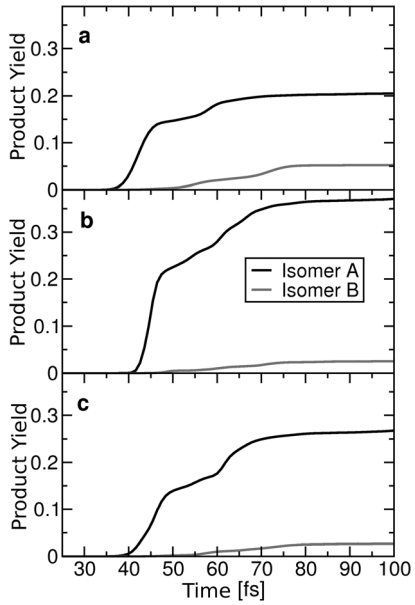

Fig. 4 Product yield with different laser pulses. The plots show the parts of the wavepacket which reach the ground state of isomers A and B respectively. (a) after excitation with a Gaussian laser pulse, (b) for the intermediate target, (c) after excitation with the optimized pulse.

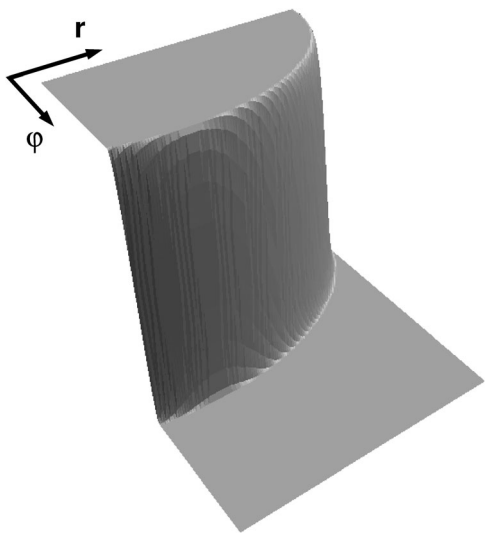

Fig. 5 Target operator for the optimization of the ground state target covering the isomer A.

feature of the system that cannot be controlled. For clarification, consider eqn (9), where the formula for the optimized field is given: The dipole moment connects the ground state of the initial wavefunction with the excited state of the target wavefunction and *vice versa*. When $\psi_i(t)$ or $\psi_f(t)$ propagate across a dark region, where the transition dipole moment is zero, the electric field becomes automatically zero, as well. Potential features inside this region therefore have only indirect influence on the optimal field.

Our experience with the ring opening in this system, where the conical intersections lie in a dark region, shows that for the straightforward target definition, *i.e.* the control target directly matches the objective, the algorithm rarely takes advantage of the conical intersections, but usually prefers the faster optical way. However, a necessary condition for the realization of the pump dump process is that at least some minor parts of the wavepacket reach the bright region (*i.e.* the region where the transition dipole moment between the two electronic states does not vanish) in the excited state in the vicinity to target isomer. This part can be dumped to the ground state and yields the desired product. The optimization leads to a laser pulse with the following features (see Fig. 6): a short pump pulse with an up chirped frequency progression is followed by an intense dump pulse which consists of two main frequencies. This laser pulse causes the following dynamics of the wave function: during the excitation process, 81% of the population is transferred to the excited state (see Fig. 6(a)) green line) where the wavefunction evolves in a very closed form towards the Franck Condon region of isomer A within few femto seconds. There it localizes and 84% of the population in the excited state is dumped to the ground state of isomer A, leading to an absolute yield of 0.66 (see Fig. 6(a)) red line). The switching is completed within only 30 fs. In our former control approach using an intermediate target, the absolute yield is just 0.27, although the relative yield of isomer A is 91%.[67] The small absolute value is mainly due to the parts of the wavepacket that remain in the excited state because this approach relies on the transfer through the conical intersections resulting in a stepwise relaxation mechanism. Here only the first step can be controlled. Later, the control of the wavepacket is lost and the natural branching ratio, which is a fundamental property of the individual CoIn, reappears. The switching is still fast, but noteably slower than the all optical realization. In the pump dump mechanism,

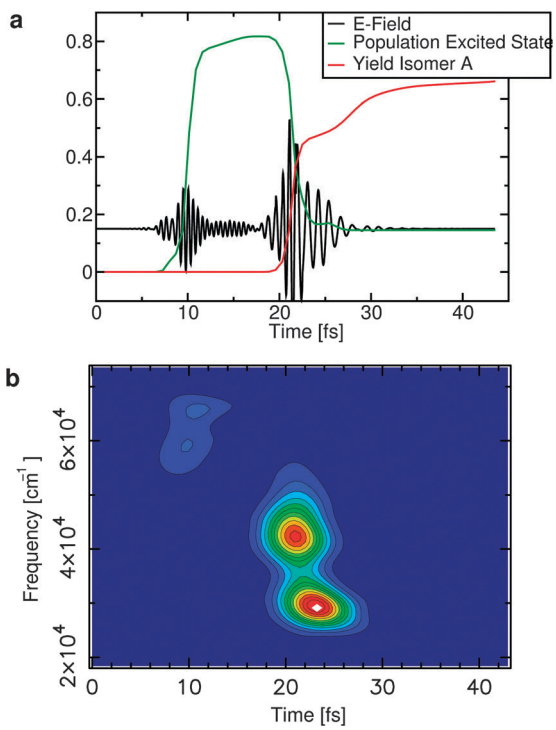

Fig. 6 (a) Temporal representation of the optimized pump dump pulse, the population in the excited state and the yield of isomer A. (b) XFROG spectrum of the optimized laser pulse depicted in (a).

the wavepacket is driven through the dark region directly to the bright region of the target isomer without crossing any CoIns. To reach the bright region, the wavepacket needs an enhanced momentum in φ, which is provided by the first subpulse of the optimal field.

3.2 OCT to control the SPODS-scheme in the potassium dimer

In the previous section, we demonstrated a control scenario, which proceeds *via* an electronic excited state. Here, we would like to review our work, where we used OCT to optimize a predefined mechanism. In addition, we present strategies that modify the OCT search space in order to favor a chosen reaction path within the optimization.

Recent developments in ultrashort laser pulse generation and shaping technology opened the door to new strategies for the control of ultrafast molecular photoreactions.[70,71] One route uses the temporal phase of the electric field as control parameter.[72] Another approach utilizes strong electric fields to shift electronic states in energy in order to steer the molecular reactions.[73] In this section we want to review our work on the selective population of dressed states (SPODS), a strategy which nicely combines both routes of phase and strong field control. SPODS can be implemented *via* the photon locking technique,[74] the optical counterpart to the spin locking technique, originally developed in NMR.[75] The photon locking technique in combination with light field control of molecular reactions was theoretically exemplified for ground state dynamics.[76]

Strong field quantum control *via* SPODS using pulse shaping techniques was experimentally demonstrated for the potassium atom by M. Wollenhaupt and T. Baumert.[77] Within their investi gations, they used sinusoidal spectral phase modulation,[78,79] chirped excitation[80] and adaptive optimization of the spectral phase[77] to realize the SPODS scheme.

In the following sections we shortly revisit the basics of the SPODS mechanism. With OCT we investigate whether the SPODS mechanism is an optimal solution for the given control task and if yes whether its efficiency can be further improved by OCT. In addition, we outline a strategy to include the SPODS mechanism in the search space of the OCT if needed by selecting special starting conditions.[81]

3.2.1 The SPODS excitation scheme. We start with a brief introduction of the excitation scheme for the SPODS mechanism on the example of K_2. The potential energy surfaces as well as the corresponding transition dipole moments, needed for our quantum dynamical simulations, were calculated with the quantum chemistry package Molpro[82] at the CASSCF(2,32) level of theory. The basis set for the description of both valence electrons consists of six s, five p, five d and two f Gaussian functions, which are sufficient to reproduce correctly the first ten atomic levels. A detailed description of this basis set including the used exponents and coefficients can be found in ref. 83. For the description of the 36 chemical invariant core electrons we used the effective core potential developed by Fuentealba *et al.*[84] for potassium. To account for the core polarization effects we also included in our calculations the core polarization potential given in ref. 85. Furthermore, we included the core core interaction for small internuclear distances as proposed by Jeung.[86] In the ideal SPODS scenario a weak and resonant pulse first creates a state of maximum coherence, *i.e.* a 50 : 50 superposition between the bare electronic states $X^1\Sigma_g^+$ and $A^1\Sigma_u^+$ (see Fig. 7 gray dash dotted arrow). This process simultaneously launches an oscillating dipole moment following the driving field with a phase shift of $\frac{\pi}{2}$.

The pre pulse is followed by an intense pulse with the same frequency. This pulse is shifted in phase by $\pm\frac{\pi}{2}$ relative to the first. Thus the electric field of the second pulse is either exactly in phase with the prepared oscillating molecular dipole or exactly shifted by π. The in phase situation selectively popu lates the lower dressed state (DS) (see Fig. 7 lower black dotted curve), the π shift leads to a selective population of the upper DS state (see Fig. 7 upper black dotted curve). During the second pulse the bare state populations are locked due to the phase relation, preventing population transfer between the $X^1\Sigma_g^+$ and $A^1\Sigma_u^+$, although the frequency is resonant on this transition.[76] Due to the laser intensity dependent energy splitting of the DS in the order of $\hbar\Omega$ with the Rabi frequency Ω (solid black arrow in Fig. 7), resonance is reached either with the $4^1\Sigma_g^+$ or the $5^1\Sigma_g^+$ target state.

With the described pulse sequence it is basically possible to control the final populations in the $4^1\Sigma_g^+$ and $5^1\Sigma_g^+$ states by switching the relative phase between the two sub pulses. In ref. 87 we showed that up to 66% of the total population can be transfered to the desired target state within the described double pulse sequence. With the help of OCT, we now investigate whether the SPODS mechanism is an optimal solution for the given control task and whether its efficiency can be further improved.

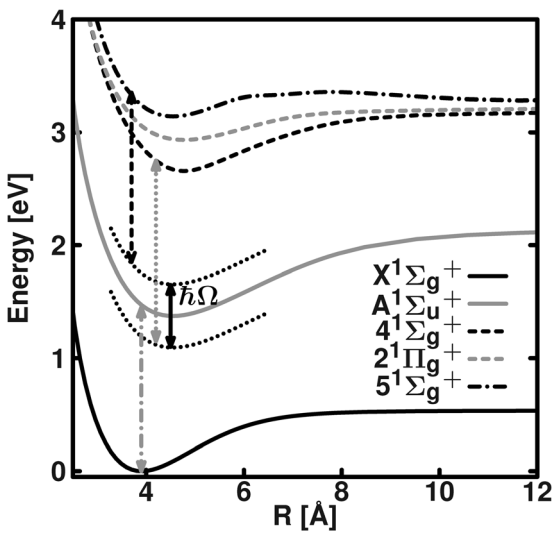

Fig. 7 SPODS scheme of potassium dimer. The first pulse in the sequence creates a superposition between the $X^1\Sigma_g^+$ and $A^1\Sigma_u^+$ states (gray dash dotted arrow). During the second pulse the $X^1\Sigma_g^+$ and the $A^1\Sigma_u^+$ states are 'photon locked'. The optical phase controls which of the dressed states (indicated as black dotted lines) energetically separated by Ω is selectively populated. Absorption of another photon leads to population transfer to either the $4^1\Sigma_g^+$ (gray dotted arrow) or $5^1\Sigma_g^+$ (black dashed arrow).

3.2.2 Optimization of the $4^1\Sigma_g^+$ target state. We started the OCT calculations with optimization for the $4^1\Sigma_g^+$ state. As target definition for OCT we use the absolute square of the expectation value of an operator $|\langle\psi(T)|\hat{O}|\psi(T)\rangle|^2$. To give the algorithm as much flexibility as possible we used projection operators $\hat{O}$, projecting the nuclear wavefunction

$$\psi(t) = \begin{pmatrix} \chi_{X^1\Sigma_g^+}(t) \\ \chi_{A^1\Sigma_u^+}(t) \\ \chi_{4^1\Sigma_g^+}(t) \\ \chi_{2^1\Pi_g^+}(t) \\ \chi_{5^1\Sigma_g^+}(t) \end{pmatrix} \quad (24)$$

on the target electronic state *e.g.* the $4^1\Sigma_g^+\left(\hat{O}_{4^1\Sigma_g^+}\right)$:

$$\hat{O}_{4^1\Sigma_g^+} = \begin{pmatrix} 0 & 0 & 0 & 0 & 0 \\ 0 & 0 & 0 & 0 & 0 \\ 0 & 0 & 1 & 0 & 0 \\ 0 & 0 & 0 & 0 & 0 \\ 0 & 0 & 0 & 0 & 0 \end{pmatrix}. \quad (25)$$

This projection operator (eqn (25)) makes the target inde pendent from the spatial shape of the wavefunction. In agree ment with SPODS only the final population of the target state is decisive. Thus additional constraints on the final wave function are avoided. For the initial laser field $\varepsilon^0(t)$ we used a Gaussian shaped pulse with a central frequency ω 911 nm, a full width at half maximum FWHM 20 fs and a maximum electric field $E_{max} = 0.0026\ \frac{GV}{cm}$. The field strength was chosen in order to start the algorithm in the weak field regime. The frequency and the FWHM were chosen in such a way that the $X^1\Sigma_g^+$ to $A^1\Sigma_u^+$ and simultaneously the $A^1\Sigma_u^+$ to $4^1\Sigma_g^+$ transition are included within the frequency spectrum of the pulse, but that the $A^1\Sigma_u^+$ to $5^1\Sigma_g^+$ transition is excluded. This initial field already populates the $4^1\Sigma_g^+$ target state up to 4%.

The optimization is performed using the OCT algorithm with a given time span of T 75 fs, a Krotov change parameter α_0 1 a.u. and the initial Gaussian shaped pulse described above. The algorithm yields a highly efficient laser field which transfers about 98.3% from the electronic and vibrational ground state to the $4^1\Sigma_g^+$ target state. The opti mized laser pulse, the induced population dynamics and the pulse characterization are shown in Fig. 8. The extracted temporal phase $\phi(t)$ (dash dotted line in Fig. 8(a)); right ordinate) clearly shows a jump of $\frac{\pi}{2}$ in the time interval between 15 and 20 fs. Right after this phase jump the $4^1\Sigma_g^+$ target state starts to be populated form the initially prepared superposition between the $X^1\Sigma_g^+$ and the $A^1\Sigma_u^+$ state (see Fig. 8(b)).

From the XFROG spectrum in Fig. 8(c) it is obvious that the algorithm used additional control knobs such as a chirp. Thus the population dynamics shows markedly higher effi ciency as it is observed with the pure double pulse sequence. From the population dynamics, the temporal phase and the shape of the optimized pulse we conclude that the OCT algorithm has found the SPODS scheme as the optimal path to selectively populate the $4^1\Sigma_g^+$ target state within the given boundary and starting conditions.

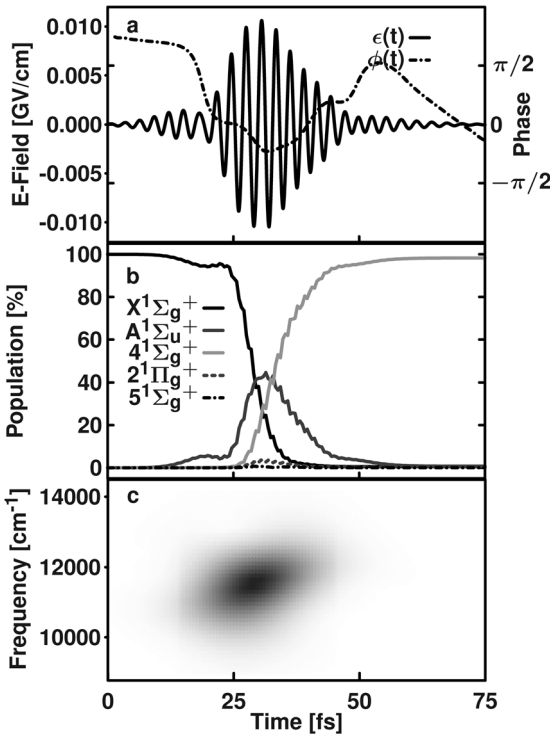

Fig. 8 Laser pulse, population dynamics and pulse characterization for the optimized SPODS mechanism. (a) Optimized pulse sequence for the selective population of the $4^1\Sigma_g^+$ target state $\varepsilon(t)$ (solid line) and its temporal phase $\phi(t)$ (dashed dotted line; right ordinate). (b) Temporal evolution of the population in the electronic states involved. (c) XFROG spectrum of the pulse sequence.

3.2.3 Optimization of the $5^1\Sigma_g^+$ target state. To optimize the pulse sequence for the upper target state we used, corre sponding to the section above, the projection operator on the $5^1\Sigma_g^+\left(\hat{O}_{5^1\Sigma_g^+}\right)$

$$\hat{O}_{5^1\Sigma_g^+} = \begin{pmatrix} 0 & 0 & 0 & 0 & 0 \\ 0 & 0 & 0 & 0 & 0 \\ 0 & 0 & 0 & 0 & 0 \\ 0 & 0 & 0 & 0 & 0 \\ 0 & 0 & 0 & 0 & 1 \end{pmatrix}. \quad (26)$$

For a first optimization we again chose a Gaussian shaped pulse with a slightly smaller FWHM compared to that in Section 3.2.2. This shorter pulse duration is needed in order to transfer a small amount of population into the target state with the initial pulse. The optimization is performed using the OCT algorithm with a given time span of T 75 fs and a carefully adjusted Krotov change parameter α_0 from 0.01 a.u. to 1 a.u.. The optimized laser pulse, the induced population dynamics and the pulse characterization are shown in Fig. 9.

The algorithm yields a highly efficient laser field which transfers about 99.2% from the electronic and vibrational ground state to the $5^1\Sigma_g^+$ target state. However, upon closer inspection, neither a simple pulse structure nor a phase evolu tion that can be easily linked to the desired SPODS mechanism can be found.

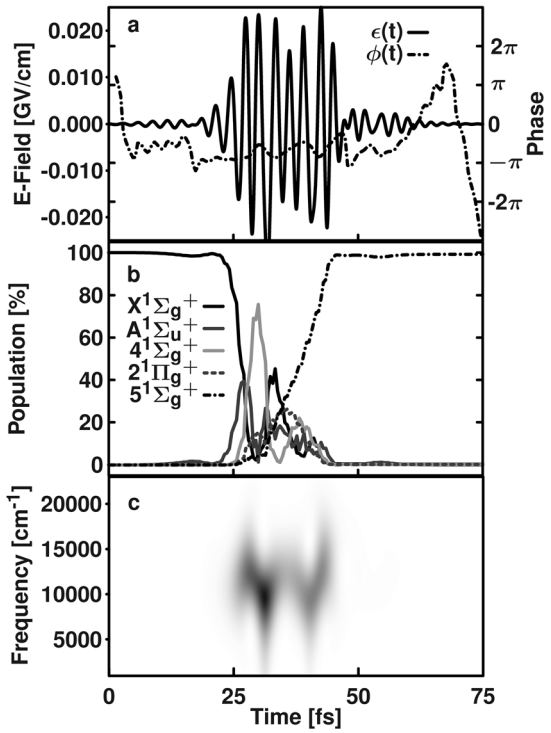

Fig. 9 Laser pulse, population dynamics and pulse characterization for the optimized SPODS mechanism using a Gaussian laser pulse as initial guess. (a) Optimized pulse sequence for the selective population of the $5^1\Sigma_g^+$ target state $\varepsilon(t)$ (solid line) and the corresponding temporal phase ($\phi(t)$; dashed dotted line; right ordinate). (b) Temporal evolution of the population in the electronic states involved. (c) XFROG spectrum of the pulse sequence.

From the SPODS mechanism we know that changing the phase shift from $\frac{\pi}{2}$ to $\frac{\pi}{2}$ leads to a selective population of the upper DS, making the $5^1\Sigma_g^+$ state accessible. Thus we inverted the sign of the temporal phase of the optimized electric field (from Section 3.2.2) to selectively populate the lower DS and reconstructed the corresponding laser field, now exhibiting a phase shift of $\frac{\pi}{2}$. Both pulses, the optimized ($\varepsilon(t)$) and the reconstructed pulse ($\varepsilon_r(t)$), together with their corre sponding temporal phase ($\phi(t)$ and $\phi_r(t)$), are shown in Fig. 10(a). Here the overall phase shift of π between the two pulses can be seen directly in the electric fields. The population dynamics, using the reconstructed electric field, is plotted in Fig. 10(b) and clearly shows the switching between the DS. After the phase shift of $\frac{\pi}{2}$ (after approx. 25 fs) now all three electronic states (*i.e.* the $4^1\Sigma_g^+$, the $2^1\Pi_g^+$ and the $5^1\Sigma_g^+$) are accessible from the upper DS within the spectral width of the laser pulse. As a result we now find a population of 6.4% in the $5^1\Sigma_g^+$ target state and a significantly reduced popula tion of 20.8% in the $4^1\Sigma_g^+$. This behavior emphasizes that the OCT algorithm has found the SPODS mechanisms in Section 3.2.2.

The further optimization for the $5^1\Sigma_g^+$ target state is performed using the OCT algorithm with the same time span as in Section 3.2.2 (T 75 fs), a Krotov change parameter α_0 1 a.u. and the reconstructed electric field $\varepsilon_r(t)$ exhibiting a phase shift of $\frac{\pi}{2}$ (see Fig. 10(a)). Again the OCT algorithm yields a highly efficient laser field which transfers about 96.7%

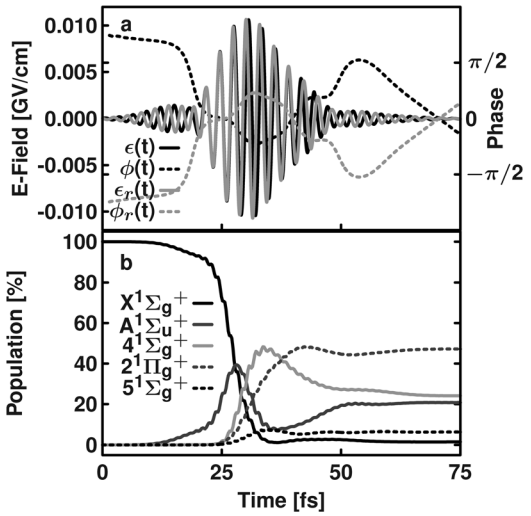

Fig. 10 (a) Optimized pulse sequence for the selective population of the $4^1\Sigma_g^+$ target state ($\varepsilon(t)$; gray solid line) and the corresponding temporal phase ($\phi(t)$; gray dashed line). Pulse sequence ($\varepsilon_r(t)$; black solid line) with reversed temporal phase $\phi_r(t)$ (black dashed line). (b) Temporal evolution of the population in the electronic states involved propagated with $\varepsilon_r(t)$.

from the electronic and vibrational ground state to the $5^1\Sigma_g^+$ target state. The resulting optimized laser pulse, the popula tion dynamics and the pulse characterization are summarized in Fig. 11. The temporal evolution of the population in the states involved (panel (b)) again shows the build up of the superposition between the $X^1\Sigma_g^+$ state and the $A^1\Sigma_u^+$ in the first 25 fs. Right after the phase jump of $\frac{\pi}{2}$ (Fig. 11(a) dash dotted line) in the time interval between 15 and 25 fs, the $5^1\Sigma_g^+$ target state gets populated up to the final value.

The comparison between the OCT solutions and the optimized double pulse sequences shows that the OCT algo rithm uses additional control knobs like a chirp to allow efficient adiabatic transitions to the target states by keeping the laser intensity as low as possible (see Fig. 8(c) and 11(c)). The direct comparison between the two optimized laser fields ($\varepsilon^{4^1\Sigma_g^+}(t)$ and $\varepsilon^{5^1\Sigma_g^+}(t)$) shows two prominent differences. The first is the π phase shift between the pulses in the time interval from 0 to 25 fs, while the two pulses are nearly in phase in the subsequent interval between 25 and 45 fs. This phase shift proves that the control of both target states achieved by the OCT follows the SPODS scheme *via* photon locking. The second difference between the two pulses is their intensity. The lower intensity is found for the $4^1\Sigma_g^+$ target state in order to suppress the competing transitions in the frequency spectrum of the pulse. Higher intensity for the $5^1\Sigma_g^+$ target state is needed, because the energies of the two target states are not symmetric around twice the energy difference between the $X^1\Sigma_g^+$ and $A^1\Sigma_u^+$ (which would be the ideal case for the SPODS scheme). Thus a higher intensity for the $5^1\Sigma_g^+$ target state is needed in order to suppress the other competing transitions in the frequency spectrum.

Based on the presented results, we can conclude that the SPODS mechanism is included in the OCT search space, and that the algorithm is able to remarkably increase the efficiency

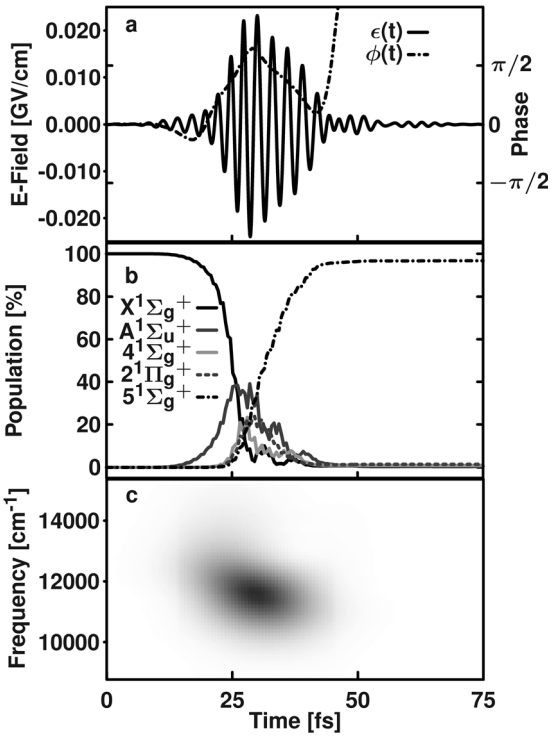

Fig. 11 Laser pulse, population dynamics and pulse characterization for the optimized SPODS mechanism using the phase reversed, optimized laser pulse for the $4^1\Sigma_g^+$ target state $\varepsilon_r(t)$ as initial guess. (a) Optimized pulse sequence for the selective population of the $5^1\Sigma_g^+$ target state (solid line) and its temporal phase $\phi(t)$ (dashed dotted line; right ordinate). (b) Temporal evolution of the population in the electronic states involved. (c) XFROG diagrams of the pulse sequence.

of the switching mechanism compared to the double pulse sequence. For the optimization of the selective population of the lower lying $4^1\Sigma_g^+$ target state, the algorithm finds the SPODS mechanism without any further constraint or addi tional starting condition as the optimal route. To optimize the selective population of the higher lying $5^1\Sigma_g^+$ target state we only needed the $\frac{\pi}{2}$ phase jump as an additional starting condi tion, in order to make the electronic state accessible within the initial guess. From the properties of the OCT algorithm it is known that high quality control and robust solutions are found even for complex quantum systems including a large number of control variables.[88] In this sense SPODS can be regarded as a robust way to control the selective population of higher lying electronic states, opening a wide spectrum of applications ranging form reaction control within molecules up to discrimination between different molecules in a mixture. For larger molecules, holding a more complex electronic structure, the frequency shaped OCT algorithm[50] might be helpful to optimize the SPODS mechanisms in order to avoid competing resonant transitions.

4 OCT to optimize transitions between vibrational states in molecules

As compared to Section 3, OCT can also be used to optimize transitions between distinct vibrational states in molecules. In this contribution, we present on the one hand results where we used such optimized laser pulses to implement quantum gates in the framework of molecular quantum computing (see Section 4.1). On the other hand, we give an example where OCT optimized pulses were used to control molecular reactions by selective excitation of vibrational eigenstates (see Section 4.2). For both applications, we compare the OCT calculations with the results of optimization algorithms working in the frequency domain and demonstrate how OCE can be modified in order to achieve simple and interpretable light pulses.

4.1 Optimizing quantum gates

Quantum information processing is a rapidly developing field and has entered different areas in physics and chemistry. The first principal ideas came from the quantum optics community and considerable success was reported with cavity quantum electrodynamics,[89] trapped ions,[90,91] and nuclear magnetic resonance (NMR).[92,93] Here the quantum systems representing the qubits are photons, atoms and the nuclear spin in molecules. The logic operations in the qubit system are performed by quantum gates. For the aim of quantum information processing a universal set of elementary quantum gates is required. Mathematically, these quantum gates are time reversible unitary transformations.

The great achievements in laser control during the last two decades have opened the connection between femtosecond lasers and quantum information processing. Modulated light fields in the femtosecond regime are able to precisely control the internal molecular degrees of freedom such as vibrations, rotations or electronic transitions.[70,94] The step from molecular reaction control to the implementation of molecular quantum gates was in this sense quite natural and opened a new direction in the field of quantum information processing. In this concept the required qubits are encoded in the internal molecular degrees of freedom, while the quantum gates (*i.e.* transitions between the pre chosen quantum states of the system) are realized by specially shaped femtosecond laser pulses.[38,95,96] This new approach has been followed by numerous studies working with internal motional states of molecules such as rovibrational states[97] and vibrational states in diatomic[98–100] and polyatomic systems.[38,95,96,101,102]

For the concept of molecular quantum computing using vibrational qubits we were able to implement a set of elemen tary quantum gates for different polyatomic systems using IR light fields. This set of gates consists of the single qubit operations NOT gate, Hadamard gate, and a phase gate (exemplarily a Π gate), as well as a controlled NOT (CNOT) gate as a two qubit operation.[96] By combining these gates we were also able to implement whole quantum algorithms, like the two qubit Deutsch Jozsa algorithm or a two qubit quantum Fourier transform.[96]

In this section we focus on the implementation of qubit operations in polyatomic systems by the use OCT. For this purpose we use the T_{1u} mode of the transition metal carbonyl complex $W(CO)_6$ as the one qubit basis and the NOT operation as the elementary gate (Section 4.1.1). $W(CO)_6$ is selected as it is also suitable for IR experiments. Vibrational ladder climbing could be shown[103] as well as selective preparation of vibrational states.[104]

In Section 4.1.2 we compare the OCT results, which are robust and have an interpretable mechanism, with the NOT operation optimized with standard genetic algorithm usually used in OCE. Based on these two benchmark calculations we demonstrate in Section 4.1.3 that alternative algorithms, which can also easily be implemented in OCE, can approach the optimal solution to a very large extent. In addition, we demonstrate that vibrational quantum gates can also be optimized *via* a non resonant Raman transition (see Section 4.1.4). For this case the frequency filtered OCT modification is needed.

4.1.1 Optimizing a NOT gate in $W(CO)_6$ using OCT. The optimization aim for the OCT algorithm is a NOT gate operation which switches the qubit basis states $|0\rangle \leftrightarrow |1\rangle$. The individual qubits are encoded in the strong IR active T_{1u} C O stretching normal mode of $W(CO)_6$. In this way, the qubit basis state $|0\rangle$ reflects the situation where the T_{1u} mode is in the vibrational ground state (ν 0), while the state $|1\rangle$ indicates that the T_{1u} mode is in the vibrational state ν 1. Consequently the NOT gate switches the populations of the vibrational states ν 0 and ν 1.

The potential energy curve of the T_{1u} mode of $W(CO)_6$ and the corresponding dipole moment are calculated quantum chemically[105] with density functional theory (b3lyp/6 31G*, LanL2DZ for W). The vibrational eigenfunctions are explicitly calculated by a relaxation method.[106] The corresponding dipole matrix elements are evaluated and the Hamiltonian is set up in the eigenstate representation. The vibrational eigenstates from the transient spectrum[104] are used to simulate the experimental conditions accurately. The energy of the higher lying vibrational levels is extrapolated with the anharmonicity traced from the spectrum. The time propagation is performed with the SPO propagator technique.

The OCT calculation for the optimization of the NOT operation was performed with a total pulse duration for the shaped OCT pulse of 5.3 ps and a penalty factor α 200. The resulting, highly efficient NOT gate laser field is presented in Fig. 12(a) and shows a simple structured electric field envelope and a moderate intensity. The induced population dynamics is drawn in Fig. 12(b) and exhibits an adiabatic and highly efficient (99.3%) switching between the basis states $|0\rangle$ (black solid line) and $|1\rangle$ (black dashed line) while the second overtone (gray dashed line) is only intermediately populated. Fig. 12(c) shows the calculated spectrum (black line) and mask functions *i.e.* the phase function as gray solid line and the transmittance function as black dashed line. Both graphs are not interpolated and correspond to a spectral pixel width of <7 cm^{-1}. A closer inspection of this figure reveals that the field is almost completely amplitude modulated and not phase shaped. The optimized pulse corresponds to a Fourier limited (FL) pulse with a FWHM of 825 fs. The spectrum is centered at the fundamental transition frequency (1983 cm^{-1}).

4.1.2 Optimizing a NOT gate in $W(CO)_6$ using genetic algorithms. In recent years, coherent control of molecular vibrational excitation with shaped mid IR pulses has been achieved.[107–111] Additionally, first methods of direct pulse shaping in this frequency regime have been developed.[104,112,113]

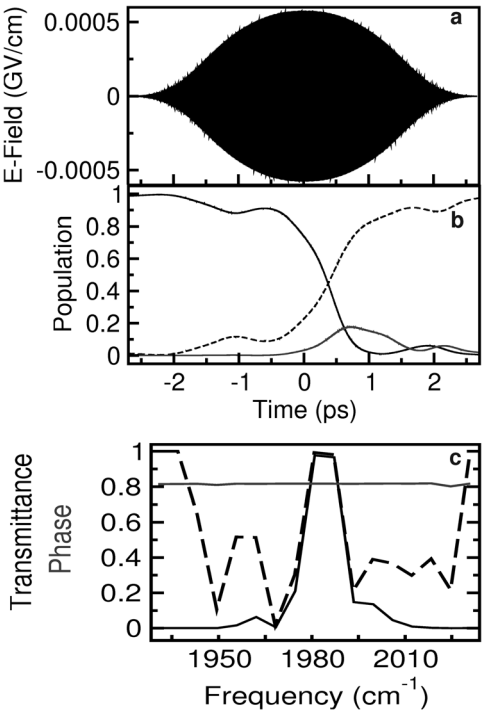

Fig. 12 Vibrational NOT gates operating on the T_{1u} mode of $W(CO)_6$, calculated with OCT. (a) Electric field with a pulse duartion of 5.3 ps. (b) Induced mechanism, where the solid black line indicates the population of the vibrational ground state, the dashed black line refers to the first excited state and the gray dashed line to the second overtone. (c) Scaled spectrum (black line), phase (gray line) and transmittance (black dashed line) functions.

This allows, together with the possibility to follow the population transfer induced by the modulated pulses,[104] for the first experimental implementation of quantum logic operations realizing molecular vibrational quantum computing operating on IR active modes.

Here, we review our investigations on the question whether and how OCE results can be traced in the OCT solution space of simple structured and short laser pulses. The focus is on similarities and differences of genetic algorithm (GA) and OCT searches and solutions found. Based on knowledge from preceding OCT studies (Section 4.1.1), the goal is to yield simple and robust GA solutions. This will enable the prediction of a promising and concerted search strategy and for optimal solutions within the control space of the experiment. Therefore we study the control and optimization prospects in the frequency domain using a GA together with the shaping of FL input pulses. The results are discussed in comparison to OCT solutions and the possible overlap of OCE and OCT solution subspaces is explored. The strategies to approach OCT solutions in OCE searches, based on GA for amplitude and phase modulation, are reviewed. In the theoretical simulation, the experimental constraints, *e.g.* the incident pulse duration, the carrier frequency, the maximum energy and the properties of the mask functions, can be met and conserved in the beginning and during the optimization.

The shaped laser fields, driving the quantum gate are optimized following the closed loop technique, which is often pursued in experiments. Here, the incident, FL pulses are

characterized by the carrier frequency ω_c, the FL pulse duration τ_p (FWHM) and the maximum intensity ε_0. With the shaping device the spectrum of the FL pulse is modulated with respect to its phase and intensity. The employed modulations in this study are, corresponding to OCE, pixeled functions for the phase and transmittance. The molecular system is then propagated under the influence of the shaped time dependent electric laser field and the quantum yield of the process is evaluated. These data are returned to the optimization algorithm, where a steady state GA from the GAlib genetic algorithm package[114] is applied in this study. For the first generation of GAs, a starting population of individuals is randomly generated, where each individual, *i.e.* each solution is described by a decision vector $x \quad (x_1, x_2, \ldots, x_n)$ in the decision or parameter space X of dimension n. The fitness of every individual is evaluated. Afterwards, a selection of the individuals is performed and they are randomly recombined and mutated to build up a new generation, which is evolving to find better solutions for the control task. Thus, good solutions remain in the population for more iterations. In a single objective algorithm the fitness is determined by assigning each solution to an objective value y in the one dimensional objective space Y according to $f{:}X \rightarrow Y$. In contrast to the optimization aim $F(\tau)$ in OCT calculations, which is a mathematical property (*e.g.* an overlap of two wavefunctions, see eqn (4)), the objective value is directly related to an experimentally measurable value. A solution $x^{(1)} \in X$ is better than another solution $x^{(2)} \in X$ if the corresponding objective value $y^{(1)} > y^{(2)}$. All solutions, existing in the parameter space X, are mapped on the objective space Y and a single optimal solution is the result of a single objective GA run. In this way, the phase and transmittance functions are optimized by the GA operators, borrowed from Darwinian evolutionary theory, to increase the efficiencies of the control processes iteratively.

In OCT calculations the pulse parameters enter in terms of a guess laser field, but they are not binding for the formalism and are generally altered during the optimization. OCT specific parameters, which need to be chosen initially, are a penalty factor for the restriction of the pulse energy and a shape function, to ensure a smooth switching on and off behavior of the pulse intensity (eqn (4)). From the optimized laser field, the required properties of the FL pulses can be deduced.[115] They can vary for runs with different penalty factors. For the GA, one has to specify the FL pulse parameters, the number of pixels and the pixel width explicitly. These parameters stay fixed during the optimization. Solutions for the selected FL pulse and pixel properties are generated exclusively. Additional GA specific input data are the mutation rate, the crossing over rate, the replacement factor, the population size and the sampling of the shaper. For the presented optimizations, the parameters 0.33 for the replacement rate, 0.05 for the mutation rate and 0.95 for the crossover rate are used.

For a meaningful comparison to the OCT results we again use the NOT gate operation in the $W(CO)_6$ complex. The pixeled phase $\phi(\omega)$ and transmittance functions $T(\omega)$ are optimized with a spectral pixel resolution of 10 cm^{-1}. The FL pulse parameters are given in Table 1, first row.

The best individual yields an efficiency of 99.6% and a rather complex envelope function, depicted in Fig. 13(a). In addition the population dynamics, plotted in the lower panel, follows a more complicated mechanism compared to OCT results (see Fig. 12). Similar structures of highly efficient quantum gates have been reported earlier for different molecules.[116–118] For more robust laser fields, the focus is on the simplification of such pulses, in favor of adiabatic state switching and low field intensities.

Table 1 FL pulse properties for the optimization of the NOT gate operations in the $W(CO)_6$ complex

τ_p/fs	ε_0/au	ω_c/cm ^{1}
105	0.002	2000
480	0.001	2000

From OCT, a certain tendency to longer FL pulses for gate operations in the carbonyl complexes is known (see Section 4.1.1). Consequently, the FWHM of the FL pulse is increased and the parameters given in Table 1, second row, are used. This optimization yields a clear simplification of the envelope function and the population dynamics as depicted in Fig. 13(b) by preserving the efficiency (99.8%). The laser field consists only of a few subpulses and is significantly shorter than the one shown in Fig. 13(a).

The results given in Section 4.1.1 and previous examinations[119] suggest that the variations within the phase functions were very small in OCT optimizations. Thus we additionally limited the maximum phase variation from $[0,2\pi]$ to $[0,0.1{\cdot}2\pi]$. The results are shown in Fig. 13(c), where a further simplification of the envelope function and the corresponding switching mechanism is observed. The efficiency of this NOT gate operation now reaches 99.9%.

These investigations lead to the assumption that fluctuating phase functions are much more probable than constant ones in GA optimizations. As these heavily varying phase functions already give good solutions, the GA has no bias for flat phase functions. No correlation is imposed on the phase values of the pixels to enforce constant phase functions, as in the case of OCT, where this is indirectly implemented by the use of high penalty factors α. Thus, the OCT optimization explores and converges in a different part of the search space compared to theoretical and experimental GA applications.

The optimization strategies presented above are based on a single objective function, which corresponds to the quantum efficiency of the investigated processes. Features like the pulse intensity may be included in the formalism as cost functions, similar to OCT (eqn (4)). The additional cost term is subtracted from the objective function in the GA optimization, however, the convergence of the quantum yield is reduced in this case. If a problem is to be studied, involving the control of several features simultaneously, multi objective algorithms, especially multi objective GAs (MOGAs), are suited for this task. In the following, we focus on our investigations utilizing MOGAs for the optimization of the NOT gate, operating on the T_{1u} mode of $W(CO)_6$. In addition, we want to show how the robust and interpretable OCT results can be approached by using such algorithms.

In multi objective optimizations, also known as multi criteria optimizations, a solution is assigned to an objective vector $y \quad (y_1, y_2, \ldots, y_k)$ with the dimensionality k, given by the

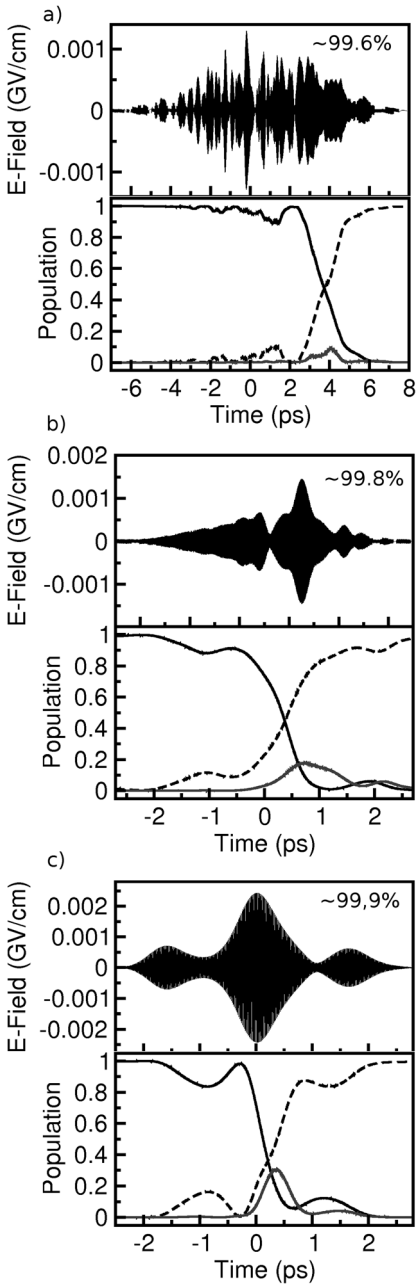

Fig. 13 Vibrational NOT gates operating on the T_{1u} mode of $W(CO)_6$, calculated with a GA. Upper panels: electric field. Lower panels: induced mechanism where the solid black line indicates the population of the vibrational ground state, the dashed black line refers to the first excited state and the gray dashed line to the second overtone. (a) Optimization with a 105 fs FL pulse. (b) Optimization using a longer (480 fs) FL pulse. (c) Optimization using a longer (480 fs) FL pulse and a limited phase variation.

number of objectives.[120] The decision which solutions are better than others is more complex and is made with the selection operator. Here, the concept of Pareto optimality (Pareto dominance relation) is applied.[120] An objective vector $y^{(1)}$ prevails all other vectors $y^{(j)}$ if no component $y_i^{(1)}$ is smaller than the corresponding components $y_i^{(j)}$ and at least one compo nent has to be larger. Such solutions are said to be non dominated and they can be mapped onto different objective vectors. Consequently, a Pareto optimal set of solutions is obtained, which build up the Pareto front in the objective space. The front represents the varying impact of the individual objec tives. In the following study, the Elitist non dominated sorting genetic algorithm II (NSGA II)[121] is applied, which has already been used in quantum control experiments.[122] Now, various supplementary constraints might be included in the NSGA II algorithm. If a solution violates a constraint, it is an infeasible solution and discarded from the set.

With this algorithm several control objectives can be maximized or minimized at the same time. In order to compare the results with the OCT calculations, we again used the NOT gate operation in the $W(CO)_6$ complex as target. Referring to the OCT optimizations, we used the quantum yield, the pulse duration and the pulse energy as additional control objectives in order to approach simple and robust pulses (see Section 4.1.1).

Fig. 14(a) shows the resulting 3D Pareto front, which is interpolated for better visualization. The highest efficiencies are shown as the red section which mark the region of gate operations that can be realized with minimal pulse energy and duration. For short pulses, the section is slightly curved, while for increasing pulse durations the pulse energy stays nearly constant. Two of the solutions from the optimal set together with the scaled spectrum and mask functions are depicted in Fig. 14(b). In the left panel, the focus is on a low pulse energy. Correspondingly, the focus is on a short pulse duration for the right panel. Both laser pulses show a very simple struc tured electric field envelope and smoothly varying phase function. Thus, by utilizing the MOGA algorithm to optimize

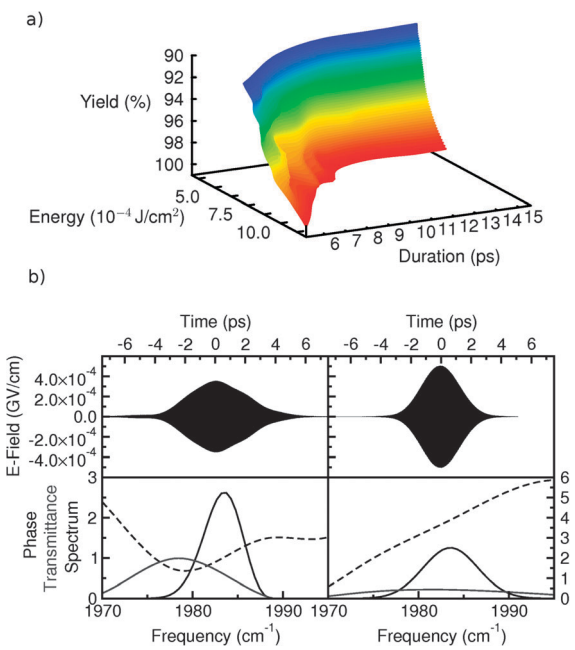

Fig. 14 (a) 3D Pareto front for NOT gates operating on the T_{1u} mode of $W(CO)_6$ with the three objectives quantum yield, pulse duration and pulse energy. (b) NOT gates, of the solutions from the optimal set. Left panel: Best laser pulse with focus on a low pulse energy together with the scaled spectrum and mask functions. Right panel: Best laser pulse with focus on a short pulse duration together with the scaled spectrum and mask functions.

the NOT gate operation, the simple structured and robust pulses obtained in the OCT calculations are approached. This means that the solution space of the MOGA and the OCT optimizations also have a lager overlap compared to the single objective GAs. Thus it will be possible to obtain robust and interpretable solutions in OCE by using MOGA optimizations.

4.1.3 Optimizing a NOT gate in $W(CO)_6$ using a modified ant colony optimization algorithm. Quantum control experiments based on computer controlled pulse modulators, working in the frequency domain, typically lead to complex pulse shapes.[21] When using pixeled mask functions, the pixel values are completely uncorrelated and can take any arbitrary values in the range [0,2π]. Distinct phase jumps between neighboring pixels are possible, which tend to generate complex laser fields, consisting of several subpulses. In addition, the strongly varying phase and transmittance functions also lead to longer pulse durations. The complex structure of such pulses limits the understanding of the underlying control mechanism. The long pulse duration favors competing decoherence processes. Ideas, circumventing the high complexities and allowing for the interpretation of the control processes, are for example based on a limitation of the phase range for each pixel or on the usage of multi objective algorithms as shown in Section 4.1.2. Both approaches have their slight drawbacks. The limitation of the phase range reduces the flexibility in the control, MOGA does not suffer therefrom, but increases the experimental effort as multiple objectives have to be measured.

In this section we review our investigations using optimizations which are based on a modified ant colony optimization (ACO) scheme. Learning from the advantages and shortcomings of the GA, it is clear that a slight correlation between neighboring pixel values has to be implemented. This implies a certain control on the complexity of the mask functions, which is directly related to the complexity of the resulting shaped laser fields. The value, each pixel takes, will still be optimized freely, but with the new method, a tunable correlation between neighboring pixels is introduced, while the flexibility of the phase is assured by avoiding strict parametrization. The optimization procedure still corresponds to a learning loop setup, but the GA is replaced by the modified ACO.

The initial laser pulse is Fourier limited with a FWHM in the range of a few hundred fs. In each iteration the ACO designs for a virtual pulse shaper a couple of mask functions for transmittance and phase. Depending on the success of the individual mask functions, their characteristics remain in the memory of the ant population in the form of a pheromone trail.[123] In contrast to the GA, the ACO algorithm uses probability functions for the transmittance p^T and the phase p^ϕ of each pixel which introduce correlation between neighboring pixels:[123]

$$p^{T_i}(\Delta T_i,n) \quad (1 \quad \beta)\tau^{T_i}(\Delta T_i,n) + \beta\eta^T(\Delta T_i), \quad (27)$$

$$p^{\phi_i}(\Delta\phi_i,n) \quad (1 \quad \beta)\tau^{\phi_i}(\Delta\phi_i,n) + \beta\eta^\phi(\Delta\phi_i). \quad (28)$$

Here i refers to the individual pixels, n is the optimization step, ΔT and $\Delta\phi$ are the transmittance and phase variation. β controls the weight of the pheromone trail activity τ and the visibility function η. For further details on the modified ant colony optimization algorithm see ref. 123 and the references therein.

To demonstrate the power of the modified ACO method, again the vibrational NOT quantum gate for the molecule $W(CO)_6$ was chosen as target. As before, the qubit basis states $|0\rangle$ and $|1\rangle$ are encoded by the vibrational ground state and first excited state of a T_{1u} symmetric mode of the carbonyl complex. For the quantum gate optimizations, a FL pulse with the carrier frequency ω_c 2000 cm^{-1}, the FWHM of the intensity profile τ_p 100 fs and the maximum energy ε_0 0.003 au 0.015 GV cm^{-1} was used. In order to achieve a fast convergence, 30 ants and 1000 iterations were used in the calculations, where only the ~30% best ants were allowed to deposit pheromone on their paths. For preferably short and simple structured laser fields a choice of the values given in Table 2 for the ACO specific parameters has proven suitable.

Fig. 15(a) (left) shows the most efficient NOT gate. The corresponding laser field stays short and exhibits a relatively simple pulse structure. For comparison of GA and ACO results, a GA run as in Section 4.1.2 is performed for the same FL pulse and with a population size of 30 and 1000 generations. The structure of the resulting GA laser field (see Fig. 15(a), right) is more complex and the pulse duration is doubled. The optimized transmittance and phase masks from the two algorithms are depicted in Fig. 15(b). For the ACO only small mask function modulations are observed (see Fig. 15(b), left). The almost constant phase function in combination with the simple transmittance function of the ACO solution (Fig. 15(b), left, black dashed line) leads to the observed uncomplex pulse structure. Such simple mask functions are seldom reached in GA runs, since there is no bias on

Table 2 ACO parameters used in the NOT gate optimization

β	ρ	σ	σ_η^T	σ_η^ϕ
0.05	0.1	0.01	0.05	0.01

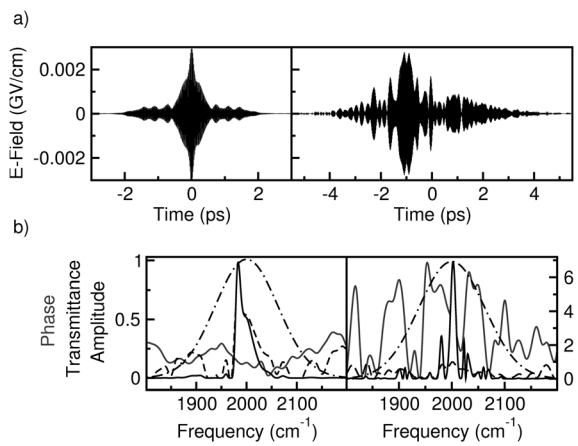

Fig. 15 (a) Best NOT gates (left: ACO, right: GA) obtained for FL pulses with τ_p 100 fs. (b) Scaled spectra of FL pulses (dashed dotted, black lines) and shaped pulses (solid, black lines), depicted in (a). The transmittance is marked as black dashed lines and the phase as gray solid lines.

small variations between the pixels. The GA optimized amplitude function (Fig. 15(b)), right, black dashed line) generates several frequency components with different phase relations, which do not enable a straightforward extraction of the mechanism.

From the above observations it becomes evident that the ACO method delivers simpler structured pulses compared to the GA solutions. In addition, they exhibit significantly shorter pulse durations. This is of high importance when efficient quantum gate operations or state to state transitions are optimized in the presence of dissipation. In addition, the information on the mechanism can already be deduced from the corresponding mask functions (see Fig. 15(b) left). Another advantage is that the ACO scheme is directly transferable to quantum control experiments and it is suggested as an alternative to GAs.[123]

4.1.4 Optimizing qubit-operations *via* a non-resonant Raman process using OCT. In the above sections we demonstrate various applications, where we used the OCT formalism to optimize different molecular processes. One fundamental difference between OCE and OCT is the spectral bandwidth of the laser field inherently present in the experiment but in principal unlimited in the original theoretical formulation. The general comparability of experimental and theoretical results may be difficult, since the theoretical answer for the optimal pulse can always span a wide bandwidth with quantum pathways out of experimental reach. Several suggestions have been made dealing with this challenge,[40,124,125] however, at the cost of monotonic convergence or general applicability.[115]

Here, we review our modified OCT approach[50] based on the Krotov method[42] (see Section 2.4) that treats time and frequency domain equally while providing monotonic convergence. This method offers an elegant possibility to study OCEs theoretically by explicitly including as a constraint the crucial experimental feature of spectral bandwidth. To demonstrate the strength of the modified OCT algorithm we implemented a highly efficient stimulated non resonant Raman quantum gate. A schematic sketch of the vibrational ladder and the controlled NOT (CNOT) gate is depicted in Fig. 16(a).

The quantum dynamics, induced by the stimulated, non resonant Raman effects, obeys the following Schrödinger equation:

$$i\frac{\partial}{\partial t}\psi(t) = \hat{H}_0\psi(t) \quad \frac{1}{2}\varepsilon_1(t)\hat{\alpha}\varepsilon_2(t)\psi(t). \qquad (29)$$

The laser molecule interaction is dependent on the two control fields $\varepsilon_1(t)$ and $\varepsilon_2(t)$. Thus, a new strategy for the simultaneous optimization of both laser pulses was developed. The multi target formulation of the OCT functional eqn (4) with the time dependent Schrödinger equations (eqn (29)) cannot be applied in this case, as the spectrum of the electric field is undefined in standard OCT search space.

As a first step the desired control objective is assumed as a simple state to state transition from the vibrational ground state (ψ_i $|00\rangle$) to the first excited state (ψ_f $|01\rangle$), as indicated in Fig. 16(a). Even if additionally one laser is kept fixed (ε_1) during the optimization with the OCT scheme (eqn (4)) and the time dependent Schrödinger equation (eqn (29)), the result will differ from the initially desired one,

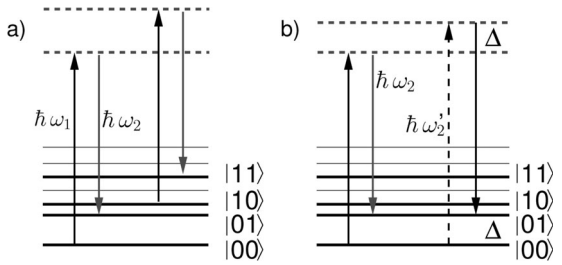

Fig. 16 Stimulated non resonant Raman quantum gates. (a) Global NOT gate indicated by the arrows $|00\rangle \leftrightarrow |01\rangle$ and $|10\rangle \leftrightarrow |11\rangle$. A CNOT gate is realized by pulses, switching the state of the active qubit when the control qubit is in state $|1\rangle$. (b) OCT optimization of a single Raman field without frequency restrictions leads to a spectrum with an additional carrier frequency ω_2' (dashed arrow) separated by 2Δ with respect to ω_2.

sketched in Fig. 16(a). This situation is visualized in Fig. 16(b), the two processes marked on the left (black and gray arrows) and on the right (dashed black and black arrows) are not distinguishable within this formalism and both paths will be used. Consequently, the spectrum of the optimized laser field ε_2 will contain two frequency components ω_2 and $\omega_2' = \omega_2 + 2\Delta$; Δ corresponds to the transition frequency $|00\rangle \rightarrow |01\rangle$. This point is not inherently problematic yet, but also does not correspond to the simplest solution of a pulse with one distinct carrier frequency, as considered in Fig. 16(a). The OCT algorithm (based on eqn (4)) completely fails, if both laser fields $\varepsilon_1(t)$ and $\varepsilon_2(t)$ are optimized simultaneously, since equivalently to the frequency component ω_2, which splits into the two components ω_2 and ω_2', in addition the spectrum of the previously fixed laser $\varepsilon_1(t)$ will also start to split into two components ω_1 and $\omega_1 + 2\Delta$. As a further progressive effect, the spectra of both laser fields will spread completely in the frequency domain.

As an answer to this problem, one has to gain control over the laser pulse spectra within the OCT formalism. To optimize such non linear, non resonant processes we used the modified implementation of OCT, which allows for strict limitations on the spectrum as presented in Section 2.4. The OCT functional is extended for the use with two different laser fields, as they appear in the Raman interaction term (eqn (29)) and takes the form:

$$\begin{aligned} &K[\psi_{fk}(t), \psi_{ik}(t), \varepsilon_1(t), \varepsilon_2(t)] \\ &= \sum_{k\ 0}^{N} \Bigg\{ |\langle\psi_{ik}(T)|\phi_{fk}\rangle|^2 \\ &\quad \sum_{1\ 1}^{2} \alpha_0 \int_0^T \frac{|\varepsilon_1(t) \quad \varepsilon_1'(t)|^2}{s(t)} \mathrm{d}t \\ &\quad \sum_{1\ 1}^{2} \gamma_1 |G_1(\varepsilon_1(t))| \quad 2\Re\Big[\langle\psi_{ik}(T)|\phi_{fk}\rangle \\ &\times \int_0^T \langle\psi_{fk}(t)|\Big[i\Big(\hat{H}_0 \quad \frac{1}{2}\varepsilon_1(t)\hat{\alpha}\varepsilon_2(t)\Big) + \frac{\partial}{\partial t}\Big]|\psi_{ik}(t)\rangle \mathrm{d}t\Big]\Bigg\}. \end{aligned} \qquad (30)$$

It includes the two laser fields $\varepsilon_l(t)$ with l 1, 2 and the time dependent Schrödinger eqn (29) with the non resonant Raman interaction. The control objective $F(\tau)$ and the temporal shape

function $s(t)$ were introduced in Section 2.4. As a consequence of the changed Hamiltonian, separate frequency constraints and pulse energy restrictions for both laser fields appear in eqn (30). By variation of the MTOCT functional (eqn (30)) with respect to the initial states $\psi_{ik}(t)$, the target states $\psi_{fk}(t)$ and the laser fields $\varepsilon_l(t)$, a set of coupled differential equations can be derived. The iterative calculation of the laser fields is performed with the Krotov method (see Section 2.4). The next iteration step $j+1$ for the laser field $\varepsilon_1(t)$ and analogously for $\varepsilon_2(t)$ can be formulated as:

$$\varepsilon_1^{j+1}(t) = \varepsilon_1^j(t) + \frac{s(t)}{2\alpha_0 N} \times \Im\left[\sum_{k\ 1}^{N} \langle\psi_{ik}(t,\varepsilon_1^j,\varepsilon_2^j)|\psi_{fk}(t,\varepsilon_1^{j+1},\varepsilon_2^{j+1})\rangle \times\langle\psi_{fk}(t,\varepsilon_1^j,\varepsilon_2^j|\hat{\alpha}\varepsilon_2^{j+1}|\psi_{ik}(t,\varepsilon_1^{j+1},\varepsilon_2^{j+1})\rangle\right] \quad \gamma_1(t), \tag{31}$$

with $\varepsilon_1^j(t)$ $\varepsilon_1'(t)$. As already discussed in Section 2.4, the Lagrange multipliers $\gamma_1(t)$ cannot be determined directly. In fact, for the calculation of $\gamma_1(t)$ the field change must be predicted in the actual iteration step. This task is performed by propagating the target states ψ_{fk} and the initial wavefunc tions ψ_{ik} with the laser fields $\varepsilon_1{}^j(t)$ from the previous iteration. The construction of the resulting fields $\gamma'_1(t)$ resembles the OCT fields of the unmodified algorithm.

$$\gamma_1'(t) = \Im\left[\sum_k \langle\psi_{fk}(t,\varepsilon_1^j,\varepsilon_2^j)|\psi_{ik}(t,\varepsilon_1^j,\varepsilon_2^j)\rangle \times\langle\psi_{fk}(t,\varepsilon_1^j,\varepsilon_2^j)|\hat{\alpha}\varepsilon_2^j|\psi_{ik}(t,\varepsilon_1^j,\varepsilon_2^j)\rangle\right]. \tag{32}$$

From here, the calculation of the laser fields for the next iteration can proceed as described in Section 2.4.

As a model system we used two strongly Raman active C H stretching vibrations of *n* butylamine. The potential energy surface as well as the polarizability tensor components were calculated with density functional theory (B3LYP/6 31++G**)[105] along both modes. The eigenfunctions and eigenvalues were explicitly evaluated by a relaxation method.[106] The quantum dynamics were carried out with a Chebychev propagation scheme.[126] Both selected modes with the fundamental frequencies ν_1 2990 cm^{-1} and ν_2 3030 cm^{-1} provide high but balanced anharmonicities (intramode Δ_1 74 cm^{-1}, Δ_2 103 cm^{-1} and intermode Δ_{12} 22 cm^{-1}), which are favorable molecular properties for vibrational quantum computing.[47] For the definition of the two qubit basis ($|00\rangle$, $|01\rangle$, $|10\rangle$, $|11\rangle$) as sketched in Fig. 16(a) we encode the vibrational ground state of each selected normal mode as the logic value 0 and the first excited state as the logic value 1.

The OCT calculations were performed in the eigenstate representation, using the 50 lowest eigenstates. For the description of the laser molecule interaction, we selected the x^2 tensor com ponent surface and evaluated the corresponding matrix elements. A universal set of quantum gates is implemented for this two qubit system by stimulated non resonant Raman processes. The CNOT gate with efficiencies above 99% is exemplarily presented in Fig. 17(a). $\varepsilon_1(t)$ and $\varepsilon_2(t)$ of the gate can be realized by simple

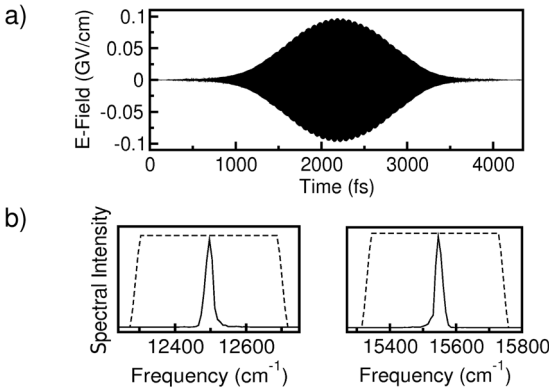

Fig. 17 The Raman fields $\varepsilon_1(t)$ and $\varepsilon_2(t)$ are depicted. Both have the same envelope functions but with different carrier frequencies. (a) Global CNOT gate laser field. (b) Spectra of both CNOT fields with their bandpass functions (dashed lines).

Gaussian shaped laser fields (compare Fig. 17(a) for $\varepsilon_1(t)$). Their related spectra are depicted together with their band pass filter functions $f_l(\omega)$ in Fig. 17(b). The carrier frequencies were chosen to be in the near IR regime with 800 nm (12 500 cm^{-1}) and 643 nm (15 541 cm^{-1}).

This OCT approach treats time and frequency domain equally and thus unifies the global optimal control with spectral constraints. This tool optimizes laser fields under realistic experimental spectral conditions. Optimal laser fields and control pathways in the experimentally accessible search space can be predicted. Additionally, an arbitrary pattern can be imprinted on the selected frequency range to suppress or enhance distinct quantum pathways. Thus, the modified OCT algorithm provides a strong and direct link to OCE.

4.2 OCT to descriminate two reactants in Grignard reactions

The nucleophilic attack of alkyl magnesium halides on a carbonyl compound traces back to Victor Grignard, a french chemist born in 1871. He was awarded with the Nobel prize of chemistry for his work on this kind of organic reaction named after its discoverer.

Grignard reactants, *i.e.* alkyl magnesium halides, are not selective, if there are two or more carbonyl groups present in the reaction mixture. In this case a complex product mixture is generated. To gain selectivity in this reaction, protection groups on all but one C O group can be introduced in a very sophisticated organic synthesis. In contrast, ultrashort IR laser pulses give the opportunity to selectively excite vibrations of only one carbonyl group in the presence of many others. By this vibrational excitation the desired carbonyl group can be stretched to the length required in the transition state of the Grignard reaction, leading to a favored attack of the reactant at this side. Therefore the laser pulse can replace the protection groups in an easy and straightforward way.

In this section we review our work on selective excitation of one carbonyl group in the presence of another one. As a model system a 1 : 1 mixture of cyclopentanone (CP) and cyclohexanone (CH) is chosen to demonstrate the powerful and highly selective discrimination between two very similar carbonyl groups.[51] In order to achieve an experimentally realizeable laser pulse with respect to its frequency components, the OCT

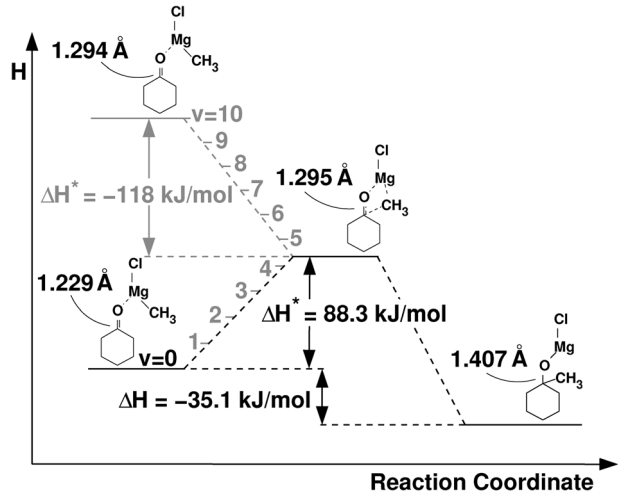

Fig. 18 Potential energy levels for the Grignard reaction of methyl magnesium chloride with CH. The vibrational excitation of the carbonyl normal mode of CH is indicated in grey. The grey numbers correspond to the vibrational levels. A qualitative identical scheme is observed for CP.[51]

algorithm with frequency restrictions is employed.[50] As Grignard reagent methyl magnesium chloride is utilized (Fig. 18).

4.2.1 Characterization of the carbonyl bonds. The C O bond length in the transition state is determined assuming a four membered ring structure in the transition state.[127–129] The displacement vectors of the normal mode leading from the transition state to the reagent and to the product indicate the elongation of the C O bond as well as the formation of the new C C bond. In the transition state the C O bond length is stretched to 1.291 Å for CP and to 1.295 Å for CH respec tively. For both molecules this corresponds to an excitation of the IR active carbonyl normal mode to a vibrational level ν 10. The initial equilibrium values are 1.225 Å (CP) and 1.229 Å (CH) respectively.

We chose the eigenstate representation of the two carbonyl stretching normal modes to perform the optimal control calculations. The potential energy curves and the dipole moments were calculated along these coordinates in CP and CH using DFT (B3LYP/6 311G**). The eigenvalues and eigenfunctions of the nuclear wavefunctions were calculated[33] and a combined Hamiltonian was set up. It consists of two diagonal blocks, one of them containing CP, $H_{ii,\mathrm{CP}}$ $\langle\psi_{i,\mathrm{CP}}|\hat{H}_0|\psi_{i,\mathrm{CP}}\rangle$, the other one containing CH, $H_{ii,\mathrm{CH}}$ $\langle\psi_{i,\mathrm{CH}}|\hat{H}_0|\psi_{i,\mathrm{CH}}\rangle$. The dipole matrix elements H_{ij} $\langle\psi_i|\hat{\mu}|\psi_j\rangle$ couple the vibrational eigenstates of each subsystem. Between the diagonal blocks no interaction exists (*i.e.* $\langle\psi_{i,\mathrm{CP}}|\hat{H}_0|\psi_{j,\mathrm{CH}}\rangle$ 0). For both molecules 20 eigenstates are taken into account, resulting in a 40 × 40 Hamiltonian matrix.

By analogy to this matrix the initial state is defined which contains a 1 : 1 mixture of CP and CH: ψ_i $c\psi^{\mathrm{CP}}_{\nu=0} + c\psi^{\mathrm{CH}}_{\nu=0}$ with the coefficient c set to $1/\sqrt{2}$. The target state ψ_t contains either CP or CH in the desired vibrational state, in this case ν 10.

In Fig. 19 the calculated spectra for CH (left) and CP (right) are shown. The fundamental frequencies of the C O stretch mode in CP and CH are seperated by only $\Delta\nu$ 28.35 cm^{-1}

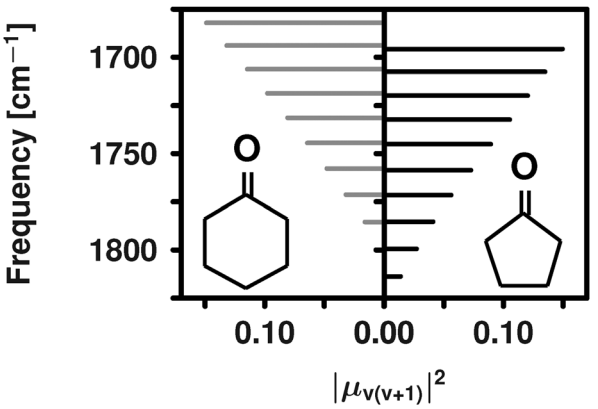

Fig. 19 Simulated spectra for CH (left) and CP (right) illustrating the transition strength for the $\Delta\nu$ 1 transitions up to $\nu_{10\leftarrow9}$. The spectra strongly interfere with each other, in particular the transition energies $E_{1\leftarrow0,\mathrm{CH}}$ and $E_{3\leftarrow2,\mathrm{CP}}$ differ by only 0.08 cm^{-1}.

(ν_{CP} 1813.72 cm^{-1} and ν_{CH} 1785.37 cm^{-1}). In addition Fig. 19 depicts the fundamental anharmonicities of both modes (14.0 cm^{-1} for the CP molecule and 13.6 cm^{-1} for the CH molecule), which are defined as the energy difference of adjacent transitions $E_{1\leftarrow0}$ $E_{2\leftarrow1}$. Note that the transition energies $E_{1\leftarrow0,\mathrm{CH}}$ and $E_{3\leftarrow2,\mathrm{CP}}$ are almost degenerate. This leads to a demanding control scheme as these two transitions cannot be addressed separately.

4.2.2 Chemoselectivity *via* selective vibrational excitation to ν = 10. The calculations were performed using the OCT algorithm with frequency restrictions. A frequency filter in the range of 1578 1875 cm^{-1}, a time window of 10 ps and a Krotov exchange parameter α_0 75 au (CP) and α_0 50 au (CH) was applied.[51] Referring to experimental conditions, the applied frequency filter defines an upper and lower bound for the spectral range of the optimized laser pulse. As a result, only the frequencies for higher overtone transi tions are suppressed. The inital laser pulse parameters were: centeral frequency ω 1746 cm^{-1} (CH) and ω 1773 cm^{-1} (CP), FWHM 3.1 ps and a maximum electric field $E_{\max} = 0.0005\,\frac{\mathrm{GV}}{\mathrm{cm}}$.

Assuming a ladder climbing mechanism, the excitation of the carbonyl normal mode of CH is a less demanding task, due to the possibility to fully suppress the spectral range of the $\nu_{1\leftarrow0,\mathrm{CP}}$ transition. Therefore the results for this control aim will be discussed first. The target state is defined as follows: ψ_t $c\psi^{\mathrm{CP}}_{\nu=0} + c\psi^{\mathrm{CH}}_{\nu=10}$.

The optimized laser field is shown in Fig. 20(a). It leads to a highly selective population transfer (Fig. 20(b)) and an overlap with the target wavefunction of ≈99.9%. For the sake of simplicity the population of the vibrational states of CH except the initial (ν_{CH} 0) and the target state (ν_{CH} 10) are added up. The underlying ladder climbing mechanism can be easily recognized.[51] The population of CP remains almost unaffected in its vibrational ground state of the C O normal mode. The corresponding spectrum of the optimized laser field together with the frequency filter is depicted in Fig. 20(c). Since the spectral range of the $\nu_{1\leftarrow0,\mathrm{CP}}$ transition is not part of the spectrum the population in ν_{CH} 0 remains untouched.

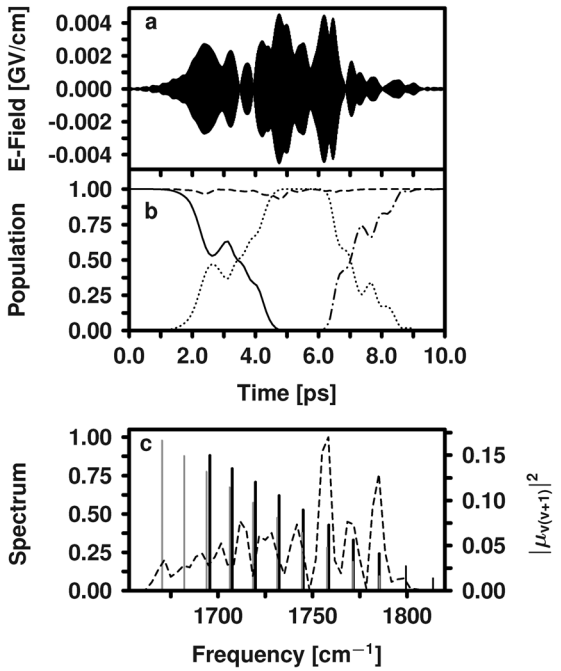

Fig. 20 (a) Optimized laser pulse with a duration of 10 ps to selectively excite CH to the vibrational level ν_{CH} 10 in the presence of CP. (b) Temporal evolution of the population P_ν of selected vibrational levels (dashed: CP ν_{CP} 0; solid: CH ν_{CH} 0; dashed dotted: CH ν_{CH} 10; dotted: CH $\sum_{\nu\neq0\neq10}P_\nu$). (c) Spectrum of the resulting laser pulse and transition strength of the calculated spectra (black: CP, grey: CH).

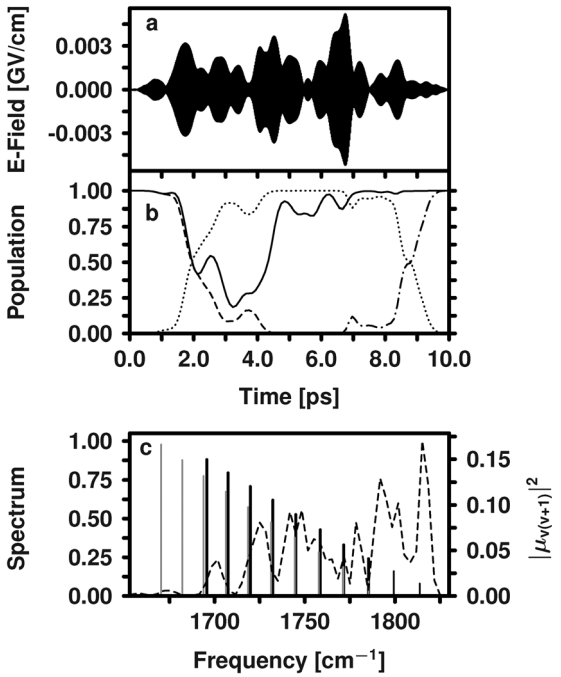

Fig. 21 (a) Optimized laser pulse with a duration of 10 ps to selectively excite CP to the vibrational level ν_{CP} 10 in the presence of CH. (b) Temporal evolution of the population P_ν of selected vibrational levels (dashed: CP ν_{CP} 0; solid: CH ν_{CH} 0; dashed dotted: CP ν_{CP} 10; dotted: CP $\sum_{\nu\neq0\neq10}P_\nu$). (c) Spectrum of the resulting laser pulse and transition strength of the calculated spectra (black: CP, grey: CH).

Optimizing the target state ψ_t $c\psi^{CP}_{\nu=10}$ + $c\psi^{CH}_{\nu=0}$ yields the laser field shown in Fig. 21(a) which delivers an overlap with the target wavefunction of ≈99.9%. This means that the population transfer to the target state is as efficient as in CH. A closer look on the induced population dynamics in Fig. 21(b) reveals changes in the transient behavior. During the first 3 ps of the pulse duration both vibrational ground states (CP and CH) are significantly depopulated. The following 3 4 ps are needed to discriminate the molecules. The CH carbonyl normal mode is driven back to the ground state, while the ladder climbing of the CP cabonyl bond is continued. During the last third of the laser pulse the desired ν 10 state of CP is populated while the population of the CH is not affected. The spectrum of the optimized laser field (Fig. 21(c)) gives clear evidence that it is not possible to suppress the spectral range of the $v_{1\leftarrow0,CH}$ transition since it is nearly degenerate with the $v_{3\leftarrow2,CP}$ transition (see Fig. 19). The latter is needed to achieve efficient population transfer in CP.

4.2.3 An alternative optimization approach *via* a modified ant colony optimization algorithm. In analogy to Section 4.1.3 we optimized the two target states ψ_t $c\psi^{CP}_{\nu=10}$ + $c\psi^{CH}_{\nu=0}$ and ψ_t $c\psi^{CP}_{\nu=0}$ + $c\psi^{CH}_{\nu=10}$ using the ACO algorithm.[123] The initial laser pulse parameters were: centeral frequency ω 1757 cm^{-1} (CH) and ω 1750 cm^{-1} (CP), FWHM 100 fs and a maximum electric field $E_{max} = 0.041 \frac{GV}{cm}$. The short pulse duration and high intensity were necessary to populate the target states to a small extent already in the first iteration. This is needed to start the ACO algorithm. The individual ACO parameters used in our optimizations are given in Table 3.

For the optimization to excite CH, a value for β of 0.02 was chosen whereas the laser pulse for the selective excitation of CP was optimized with β 0.07. In both cases, the pheromone trail persistance ρ is 0.5 and the standard deviation around the phase and transmittance variation values of each ant is 0.01. Slightly different values for the standard deviation of the probability of larger transmittance σ^T_η and phase variations σ^ϕ_η between neighbouring pixels are used.[123]

All optimizations with the ACO algorithm were done within 1000 iterations. During each iteration 60 ants chose their individual transmittance and phase variation values for each pixel. Due to the complexity of the investigated control task only the 5% best ants deposit pheromone on the trail.

Fig. 22(a) shows an optimized laser pulse for the excitation of CH to the vibrational level ν_{CH} 10. It leads to an overlap with the target states of ≈94.2%. Although the efficiency of the laser field is slightly smaller than that of the OCT optimized pulse (see Fig. 20), again CP is unaffected and stays in its vibrational ground state. The induced population dynamics are depicted in Fig. 22(b) and show the population transfer to

Table 3 ACO parameters used for the optimization of laser pulses to selectively excite CH and CP in a 1 : 1 mixture respectively

	β	ρ	σ	σ^T_η	σ^ϕ_η
CH	0.02	0.5	0.01	0.3	1.5
CP	0.07	0.5	0.01	0.5	1.0

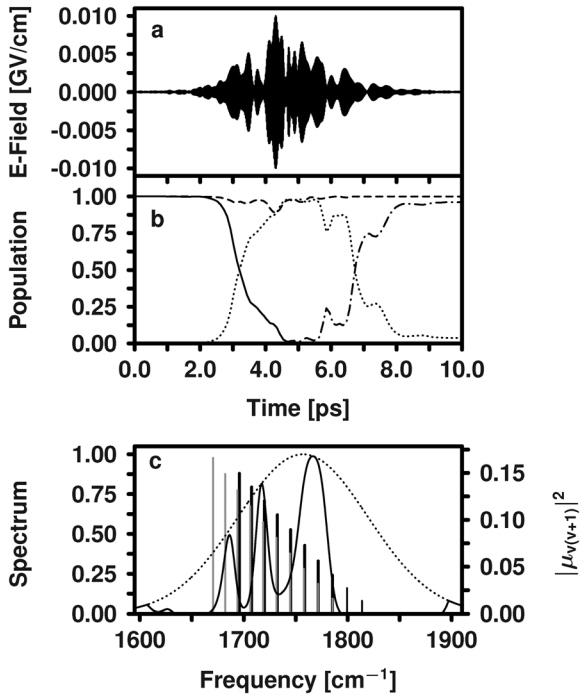

Fig. 22 (a) Optimized laser pulse (ACO algorithm) with a duration of 10 ps to selectively excite CH to the vibrational level ν_{CH} 10 in the presence of CP. (b) Temporal evolution of the population P_ν of selected vibrational levels (dashed: CP ν_{CP} 0; solid: CH ν_{CH} 0; dashed dotted: CH ν_{CH} 10; dotted: CH $\sum_{\nu\neq0\neq10}P_\nu$). (c) Spectrum of the resulting laser pulse (solid line) and transition strength of the calculated spectra (black: CP, grey: CH). The dotted line indicates the spectrum of the Fourier limited input pulse with a FWHM of 100 fs.

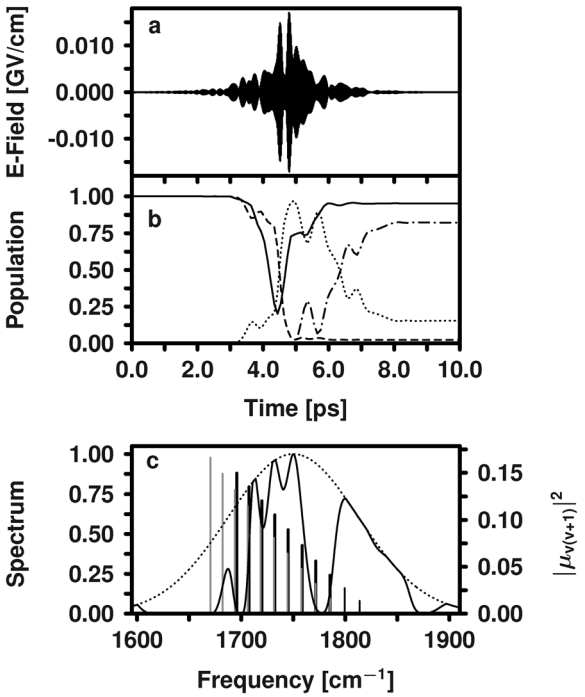

Fig. 23 (a) Optimized laser pulse (ACO algorithm) with a duration of 10 ps to selectively excite CP to the vibrational level ν_{CP} 10 in the presence of CH. (b) Temporal evolution of the population P_ν of selected vibrational levels (dashed: CP ν_{CP} 0; solid: CH ν_{CH} 0; dash dotted: CP ν_{CP} 10; dotted: CP $\sum_{\nu\neq0\neq10}P_\nu$). (c) Spectrum of the resulting laser pulse (solid line) and transition strength of the calculated spectra (black: CP, grey: CH). The dotted line indicates the spectrum of the Fourier limited input pulse with a FWHM of 100 fs.

the target state of CH (ν_{CH} 10) of $\approx$0.96. The effective pulse duration of 7 ps is slightly shorter than in the case of the OCT optimization, while the maximum electric field is correspond ingly higher. Consequently, the excitation mechanism is more complex. Nevertheless, the explicit population dynamics (collectively shown as dotted black line) reveal the underlying ladder climbing mechanism up to the vibrational level ν_{CH} 5. The depicted spectrum of the optimized laser field in Fig. 22(c) (solid line) shows that the ACO algorithm suppresses, in agreement with the OCT results, the vibrational frequencies around the $\nu_{1\leftarrow0,CP}$ transition. In addition, Fig. 22(c) shows the spectrum of the Fourier limited input pulse as a black dotted line.

Again, the more challenging control scenario is the selective excitation of the C O normal mode of CP in the mixture. In Fig. 23(a) the optimized pulse is depicted, which also leads to a selective population of the desired target state (see Fig. 23(b)). Compared to the OCT result (see Fig. 21) the pulse again is approx. 4 ps shorter with a higher maximum electric field. The realized mechanism for the population transfer (shown in Fig. 23(b)) is more sophisticated compared to the OCT result. The ACO pulse first depopulates the ground state of CH and subsequently drives the CP ladder to the vibrational level ν_{CP} 2. After about 4.5 ps the pulse simultaneously induces the $\nu_{3\leftarrow2,CP}$ transition as well as the back transfer of CH into its ground state. Note that this is approximately the same time interval, in which OCT discriminates between the two species. Afterwards the population of CP is quickly driven to the level ν_{CP} 10. The final population of CH in the target state is approx. 0.92 while CH is nearly quantitavely driven back to the ground state ($\approx$0.95). The spectrum of the optimized laser pulse (see Fig. 23(c)) has a comparatively high intensity in the spectral range of the $\nu_{1\leftarrow0,CH}$ transition. In contrast to OCT the ACO algorithm here tries to suppress the frequencies around the $\nu_{2\leftarrow1,CH}$ transition to avoid further excitation of CH, which obviously leads to comparably results by utilizing different mechanisms.

5 Outlook and conclusions

In the field of reaction control a new powerful control knob could be added by the realization of phase stable few femto second light pulses. The idea is to directly control a molecular reaction by preparing and steering electronic wavepackets inside a molecule.[130,131] From the theory side, the question arises whether OCT is able to treat such control or not? The following outlook, which contains preliminary results on this topic, is dedicated to answer this sort of upcoming questions.

5.1 Outlook: OCT to control electronic wavepackets

In this section we apply OCT to control electronic wavepackets. The control directly links to the optimization of a superposition between electronic states with a distinct phase relation. For read out of the prepared phase, the electronic wavepacket is

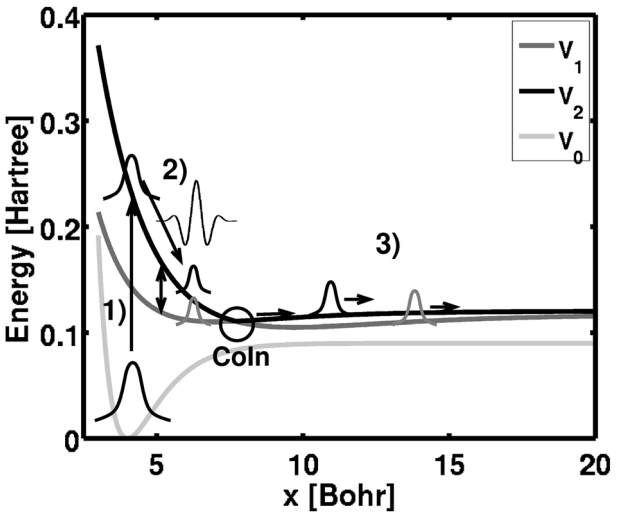

Fig. 24 Schematic representation of the investigated dynamic in side view: (1) an ultrashort laser pulse excites the wavepacket from the ground state V_0 to the excited state V_2. (2) While the wavepacket moves towards the conical intersection a laser pulse creates a super position between the two crossing states. Through the coupling at the conical intersection the superposition of the wavepackets vanishes. (3) According to the phase of the laser the wavepacket is on state V_1 or V_2 after the conical intersection.

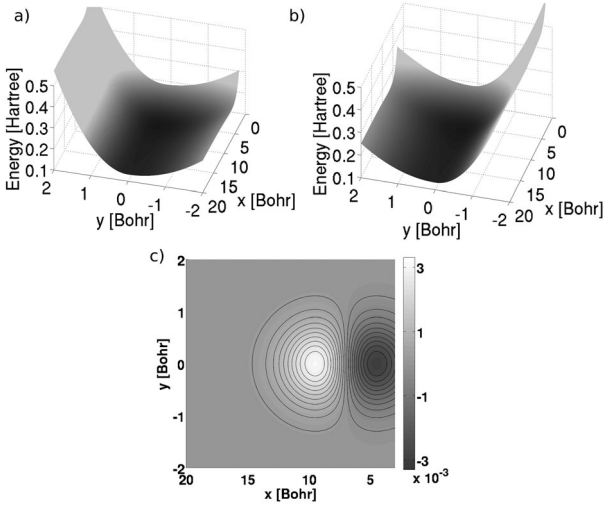

Fig. 25 (a) Potential energy surface S_1 in diabatic representation. (b) Potential energy surface S_2 in diabatic representation. (c) Diabatic coupling element H_{12}.

sent through a CoIn. This translates the phase of the super position into a specific population ratio between the electronic states.[87] This control is reached within the framework of OCT by using phase sensitive targets for each electronic state included in the superposition. To benchmark the capabilities of algorithm we implemented the mechanism shown in Fig. 24. The starting condition is prepared by photo excitation from the vibrational ground state in V_0 to the upper potential V_2 (see Fig. 24 step (1)). As control aim serves the superposition of the two intersecting potentials V_2 and V_1. The spatial position of the target is chosen just before the coupling region (see Fig. 24 step (2)). After the target wavepacket has passed through the CoIn (see Fig. 24 step (3)), the imprinted electronic phase can be read out from the population ratio. In the following we will first introduce the used model system in Section 5.1.1. Subsequently, we discuss the results in Section 5.1.2.

5.1.1 Model system. The model system is similar to that in ref. 132 and consists of three two dimensional diabatic potential energy surfaces (S_0, S_1 and S_2) with a diabatic coupling H_{12} between the energetic higher lying potentials S_1 and S_2 (see Fig. 25). The individual electronic surfaces S_0, S_1 and S_2 are given by the following analytical equations:

$$S_1 = \begin{cases} D(1 \quad e^{-b(x-r)})^2 + \frac{1}{2}k_1y^2, & \text{for } y \le 0 \\ D(1 \quad e^{-b(x-r)})^2 + \frac{1}{2}k_2y^2, & \text{for } y > 0 \end{cases} \tag{33}$$

$$S_2 = \begin{cases} D(1 \quad e^{-b(x-r)})^2 + \frac{1}{2}k_2y^2, & \text{for } y \le 0 \\ D(1 \quad e^{-b(x-r)})^2 + \frac{1}{2}k_1y^2, & \text{for } y > 0 \end{cases} \tag{34}$$

$$S_0 \quad D_0\,(1 \quad e^{-b_0(x-y_0)})^2 \; + \; \tfrac{1}{2}\,k_0y^2 \tag{35}$$

The potentials exhibit a Morse potential in the x direction and a harmonic potential along y. To lift the degeneracy along the x coordinate we use a two dimensional Gaussian shaped diabatic coupling element centered at y y_c; x x_c and a zero crossing along x at x x_c:

$$H_{12} \quad \gamma(x \quad x_c)e^{-\beta_1(x-x_c)^2}e^{-\beta_2(y-y_c)^2} \tag{36}$$

The parameter γ influences the strength of the diabatic coupling and $\beta_{1/2}$ the width of the Gaussian in x and y direction. The harmonic constants k_1 and k_2 define the slope of the potentials in the y direction. For a system that can be triggered by a UV pump and controlled by an IR pulse we use the parameters in Table 4. The quantum dynamical calcu lations are carried out on adiabatic potentials. This represen tation has the advantage that more than one CoIn or even a seam of CoIns can be included in the dynamics.

For the transformation of the diabatic potentials into the adiabatic representation we need the mixing angle θ which is defined by

$$\cos(2\theta) = \frac{\Delta H}{\sqrt{\Delta H^2 + H_{12}^2}}, \; \sin(2\theta) = \frac{H_{12}}{\sqrt{\Delta H^2 + H_{12}^2}}, \tag{37}$$

with $\Delta H = \frac{S_1 - S_2}{2}$. The transformation of the diabatic poten tials S_1, S_2 into the adiabatic potentials V_1 and V_2 by using the mixing angel θ is finally given by:

$$\begin{pmatrix} V_1 \\ V_2 \end{pmatrix} = \begin{pmatrix} \cos(\theta) & \sin(\theta) \\ \sin(\theta) & \cos(\theta) \end{pmatrix} \begin{pmatrix} S_1 \\ S_2 \end{pmatrix}. \tag{38}$$

As no coupling occurs with the diabatic ground state S_0 the adiabatic surface V_0 is equal to S_0. In the adiabatic

Table 4 Parameters used for the model system to get a preferably realistic system

D_0	0.09	r_0	4	b_0	0.9
D	0.012	r	7	b	0.36
k_0	0.0747	k_1	0.22	k_2	0.06
γ	0.001	β_1	0.05	β_2	1.5
m_x	22680.43	m_y	10000		
x_c	7.0	y_c	0		

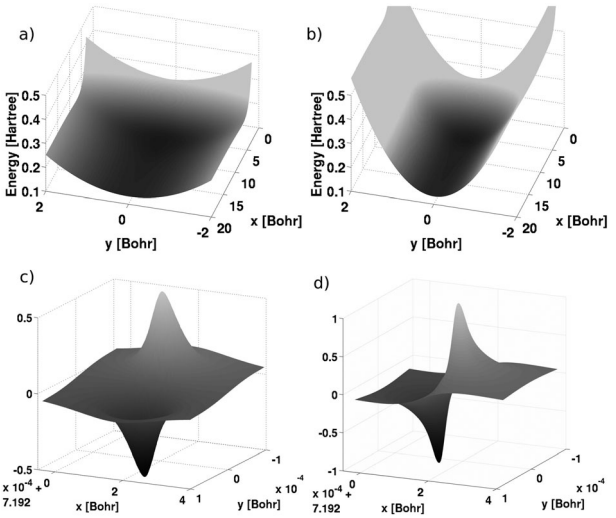

Fig. 26 (a) Potential energy surface V_1 in adiabatic representation. (b) Potential energy surface V_2 in adiabatic representation. (c) Non adiabatic coupling element $f_{12}^{(x)}$ in the x direction. (d) Non adiabatic coupling element $f_{12}^{(y)}$ in the y direction.

representation the two excited potentials only degenerate at the CoIn which is located at x x_c, y y_c. In our model system, the branching vectors of the CoIn (g/h vectors) and the reactive coordinates x and y span the same plane. The two adiabatic potentials are depicted in Fig. 26(a) and (b). The corresponding non adiabatic coupling elements $f_{12}^{(x)}$ and $f_{12}^{(y)}$ can be calculated from the mixing angle according to:

$$\langle \Phi_i^{\text{adiab}} | \partial_k \Phi_j^{\text{adiab}} \rangle \quad \langle \cos(\theta)\Phi_i^{\text{diab}} + \sin(\theta)\Phi_j^{\text{diab}} | \partial_k (\sin(\theta)\Phi_i^{\text{diab}} + \cos(\theta)\Phi_j^{\text{diab}}) \rangle \quad \cos^2(\theta)\partial_k\theta \quad \sin^2(\theta)\partial_k\theta \quad \partial_k\theta, \tag{39}$$

and are shown in Fig. 26(c) and (d). Here, $\vec{g}$ and $\vec{h}$ are perpendicular, both coupling elements ($f_{12}^{(x)}$ and $f_{12}^{(y)}$) exhibit a sign change at the CoIn along the y and x direction, respectively. Note, if $\vec{g}$ and $\vec{h}$ are not perpendicular the sign of the coupling elements would change also at the CoIn, but the enclosed angle between the nodal planes will differ.

For the quantum dynamical calculations we used a grid with 600 points ranging from 3 to 20 in the x direction and 256 points ranging from 2 to 2 in the y direction. In addition we assume no kinetic coupling between the coordinates x and y. Thus the kinetic Hamiltonian can be written as:

$$\hat{T}_{\text{nuc}} = \frac{1}{2m_x}\frac{\partial^2}{\partial x^2} \quad \frac{1}{2m_y}\frac{\partial^2}{\partial y^2} \tag{40}$$

We found that the sign change of the relevant non adiabatic coupling element (NACME) along the nuclear coordinates is imprinted on to the phase of the electronic wavefunction during the non adiabatic population transfer. This is related to the Berry phase.[133] To be able to monitor the relative phase of the target electronic wavepacket from the population branching after the CoIn this sign change induced by the NACME has to be compensated in advance. Thus the electronic wavefunctions forming the superposition need a sign change in the same direction as the NACME. This can be achieved during laser excitation. In general, the formation of the target superposition depends on the interplay between the electric field and the transition dipole moment coupling V_1 and V_2. The needed sign change along the nuclear coordinates can only arise through the transition dipole moment. To extract the sign change, we transform the adiabatic dipole moment $\langle \Phi_1^{\text{adiab}} | \mu | \Phi_2^{\text{adiab}} \rangle$ into the diabatic basis:

$$\langle \Phi_1^{\text{adiab}} | \mu | \Phi_2^{\text{adiab}} \rangle \quad \langle \cos(\theta)\Phi_1^{\text{diab}} + \sin(\theta)\Phi_2^{\text{diab}} | \mu | \sin(\theta)\Phi_1^{\text{diab}} + \cos(\theta)\Phi_2^{\text{diab}} \rangle \quad \cos^2(\theta)\langle \Phi_1^{\text{diab}} | \mu | \Phi_2^{\text{diab}} \rangle \quad \sin^2(\theta)\langle \Phi_2^{\text{diab}} | \mu | \Phi_1^{\text{diab}} \rangle \quad \cos(2\theta)\langle \Phi_1^{\text{diab}} | \mu | \Phi_2^{\text{diab}} \rangle. \tag{41}$$

As can be seen from eqn (37), the sign of $\cos(2\theta)$ changes with the sign of ΔH while the diabatic electronic wavefunction preserves its character by definition. Thus the adiabatic transition dipole moment changes sign like ΔH. In our model system this occurs parallel to the x direction and the laser coupling induces the desired sign change in the electronic wavefunction along the y axis, compensating the sign change of the NACME.

5.1.2 Control of the relative phase within an electronic wavepacket using OCT. OCT is used to control the phase of an electronic wavepacket. Fig. 27 shows schematically the processes of this control scheme. Starting from a wavepacket on the V_2 potential which is prepared by an ultrashort laser pulse from the ground state (Fig. 24 step (1)) the OCT algorithm is asked to create the desired phase sensitive superposition of the states V_1 and V_2 just before the CoIn is reached. During the laser coupling the phase change in the transition dipole moment imprints the required sign change in the V_1 electronic wavefunction (see Fig. 27 step (2)). Afterwards the superposition state reaches the CoIn and the prepared relative electronic phase is translated into population branching between the states V_1 and V_2 (see Fig. 27 step (3)).

To assure that the pulse ends approx. 40 fs after the beginning of the propagation, right before the CoIn is reached, a Gaussian shape function $s(t)$ is used and the Krotov change parameter α_0 was set to 625 a.u.. To compute the time evolution we use the Chebychev propagator scheme[134] with a time step of 0.097 fs. As control target we chose a superposition with a relative phase of 0π.

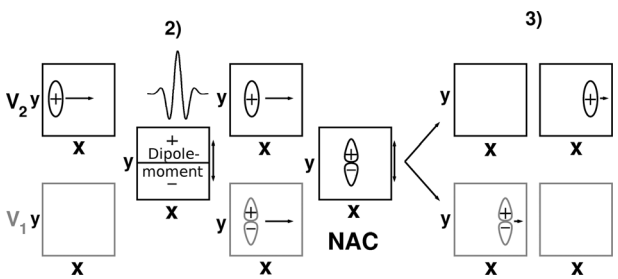

Fig. 27 Schematic representation of the control scheme (the steps correspond to Fig. 24). Step (2): Build up of the superposition between electronic states V_1 and V_2 imprinting the sign change onto the electronic wavefunction (in V_1) along the y axis. Step (3): After the system has passed the CoIn, the prepared relative phase in the superposition can be read out from the population branching. This is possible, as the inprinted sign change and the sign change of the NACME cancel each other.

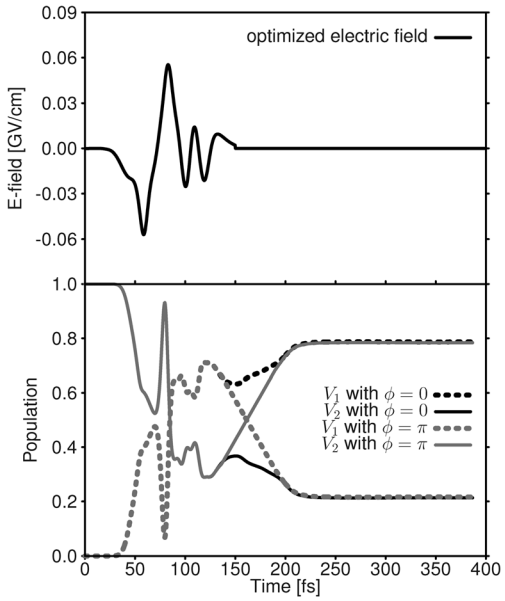

Fig. 28 (Top) Optimized laser pulse to create the phase sensitive superposition between the electronic states V_1 and V_2 before the conical intersection. (Bottom) Population dynamics with (gray) and without phase change (black) of the optimized laser pulse.

Fig. 28 shows the optimized electric field yielding to a target overlap of 0.63 (top panel). The induced population dynamics in the V_1, V_2 subsystem is depicted in the bottom panel (solid black and dashed black lines). The reached target overlap translates into a population ratio $V_1 : V_2$ of 79 : 21. Shifting the phase of the electric field by π changes the relative phase of the superposition by π accordingly. The result is a complete inversion of the initial branching ratio. This is depicted in Fig. 28 bottom panel (solid gray and dashed gray lines).

The bottom line is that direct control of electronic wave packets *via* the absolute phase of the electric field is included within the solution space of OCT. The resulting laser field is complex structured few cycle pulses reflecting the highly demanding control task.

5.2 Conclusion

In this perspective we summarized the results from our various OCT studies, ranging from reaction control over quantum information to the control of electronic motion, highlighting the enormous flexibility of the algorithm. One of our main emphases has always been the connection between theory and experiment. This is the driving force for our ongoing developments in the research topic of coherent control. In this spirit we presented modifications and extensions of the OCT functional to meet the experimental requirements. On the other hand, we explored theoretically the experimental search space, to pinpoint their similarities and differences. Based on these results, we outlined strategies to align both search spaces. To introduce the spectral bandwidth of the laser pulses used in the experiments, we included frequency filtering in the OCT formalism. As an alternative to a reduction of the parameter space through *e.g.* analytic phase masks, often used in experiments to obtain interpretable light fields and control mechanisms, we showed that a sophisticated enhancement of the search space fulfills these goals. Replacement of the conventional genetic algorithm by the multi objective genetic algorithm is one route. Swarm intelligence, as realized by the modified ant colony optimization algorithm, is another way. Both implementations preserve the full flexibility during the experimental search. All these modifications can be regarded as a major step towards the realization and interpretation of complex control tasks. From a present day perspective, the most complex control task encompasses the simultaneous control of electron and nuclear motion. Our very recent example demonstrates that this can be achieved again within the framework of OCT. The resulting light fields need the capabilities of light wave form synthesis, a forefront research topic in attosecond science.[135]

Acknowledgements

The authors would like to thank Caroline Gollub, Dorothee Geppert and Lena Seyfarth for their contributions to the present work. We are also grateful for support by the DFG *via* the Cluster of Excellence: Munich Centre of Advanced Photonics, the SFB749 and the Normalverfahren. We appreciate the Leibnitz Rechenzentrum der Bayrischen Akademie der Wissenschaften (LRZ) for allocation of computing time.

References

1 P. Brumer and M. Shapiro, *Chem. Phys. Lett.*, 1986, **126**, 541.
2 M. Shapiro, J. W. Hepburn and P. Brumer, *Chem. Phys. Lett.*, 1988, **149**, 451.
3 U. Gaubatz, P. Rudecki, M. Becker, S. Schiemann, M. Kulz and K. Bergmann, *Chem. Phys. Lett.*, 1988, **149**, 463 468.
4 U. Gaubatz, P. Rudecki, S. Schiemann and K. Bergmann, *J. Chem. Phys.*, 1990, **92**, 5363 5376.
5 D. J. Tannor and S. A. Rice, *J. Chem. Phys.*, 1985, **83**, 5013 5018.
6 D. J. Tannor, R. Kosloff and S. A. Rice, *J. Chem. Phys.*, 1986, **85**, 5805 5820.
7 E. D. Potter, J. L. Herek, S. Pedersen, Q. Liu and A. H. Zewail, *Nature*, 1992, **355**, 66.
8 A. H. Zewail, *J. Phys. Chem. A*, 2000, **104**, 5660 5694.
9 R. S. Judson and H. Rabitz, *Phys. Rev. Lett.*, 1992, **68**, 1500 1503.
10 H. Rabitz, R. de Vivie Riedle, M. Motzkus and K. L. Kompa, *Science*, 2000, **288**, 824 828.
11 A. Weiner, D. Leaird, J. Patel and J. I. Wullert, *IEEE J. Quantum Electron.*, 1992, **28**, 908 920.
12 C. J. Bardeen, V. V. Yakovlev, K. R. Wilson, S. D. Carpenter, P. M. Weber and W. S. Warren, *Chem. Phys. Lett.*, 1997, **280**, 151 158.
13 A. Assion, T. Baumert, M. Bergt, T. Brixner, B. Kiefer, V. Seyfried, M. Strehle and G. Gerber, *Science*, 1998, **282**, 919 922.
14 R. J. Levis and H. Rabitz, *J. Phys. Chem. A*, 2002, **106**, 6427 6444.
15 R. A. Bartels, T. C. Weinacht, S. R. Leone, H. C. Kapteyn and M. M. Murnane, *Phys. Rev. Lett.*, 2002, **88**, 033001.
16 G. Vogt, G. Krampert, P. Niklaus, P. Nuernberger and G. Gerber, *Phys. Rev. Lett.*, 2005, **94**, 068305.
17 L. Polachek, D. Oron and Y. Silberberg, *Opt. Lett.*, 2006, **31**, 631 633.
18 M. Plewicki, S. Weber, F. Weise and A. Lindinger, *Appl. Phys. B: Lasers Opt.*, 2007, **86**, 259 263.
19 D. Zeidler, S. Frey, K. L. Kompa and M. Motzkus, *Phys. Rev. A: At., Mol., Opt. Phys.*, 2001, **64**, 023420.
20 J. L. Herek, W. Wohlleben, R. J. Cogdell, D. Zeidler and M. Motzkus, *Nature*, 2002, **417**, 533.
21 T. Hornung, R. Meier and M. Motzkus, *Chem. Phys. Lett.*, 2000, **326**, 445 453.
22 D. Meshulach and Y. Silberberg, *Nature*, 1998, **396**, 239 242.

23 V. V. Lozovoy, I. Pastirk, K. A. Walowicz and M. Dantus, *J. Chem. Phys.*, 2003, **118**, 3187 3196.
24 A. Bartelt, A. Lindinger, C. Lupulescu, Š. Vajda and L. Woste, *Phys. Chem. Chem. Phys.*, 2003, **5**, 3610 3615.
25 M. Wollenhaupt, A. Prakelt, C. Sarpe Tudoran, D. Liese, T. Bayer and T. Baumert, *Phys. Rev. A: At., Mol., Opt. Phys.*, 2006, **73**, 063409.
26 G. Vogt, P. Nuernberger, R. Selle, F. Dimler, T. Brixner and G. Gerber, *Phys. Rev. A: At., Mol., Opt. Phys.*, 2006, **74**, 033413.
27 J. Roslund and H. Rabitz, *Phys. Rev. A: At., Mol., Opt. Phys.*, 2009, **80**, 013408.
28 A. P. Peirce, M. A. Dahleh and H. Rabitz, *Phys. Rev. A: At., Mol., Opt. Phys.*, 1988, **37**, 4950 4964.
29 R. Kosloff, S. Rice, P. Gaspard, S. Tersigni and D. Tannor, *Chem. Phys.*, 1989, **139**, 201 220.
30 W. Zhu, J. Botina and H. Rabitz, *J. Chem. Phys.*, 1998, **108**, 1953 1963.
31 W. Zhu and H. Rabitz, *J. Chem. Phys.*, 1998, **109**, 385 391.
32 D. J. Tannor, V. Kazakov and V. Orlov, *Time Dependent Quantum Molecular Dynamics*, 1992, pp. 347 360.
33 K. Sundermann and R. de Vivie Riedle, *J. Chem. Phys.*, 1999, **110**, 1896 1904.
34 V. Bonačič Koutecký and R. Mitrić, *Chem. Rev.*, 2005, **105**, 11 66.
35 B. Amstrup, R. J. Carlson, A. Matro and S. A. Rice, *J. Phys. Chem.*, 1991, **95**, 8019 8027.
36 M. Baer and R. Englman, *Chem. Phys. Lett.*, 1997, **265**, 105 108.
37 F. Shuang and H. Rabitz, *J. Chem. Phys.*, 2006, **124**, 154105.
38 C. M. Tesch and R. de Vivie Riedle, *Phys. Rev. Lett.*, 2002, **89**, 157901.
39 J. Manz, K. Sundermann and R. de Vivie Riedle, *Chem. Phys. Lett.*, 1998, **290**, 415 422.
40 P. Gross, D. Neuhauser and H. Rabitz, *J. Chem. Phys.*, 1992, **96**, 2834.
41 S. Shi, A. Woody and H. Rabitz, *J. Chem. Phys.*, 1988, **88**, 6870.
42 J. Somloi, V. A. Kazakov and D. J. Tannor, *Chem. Phys.*, 1993, **172**, 85 98.
43 J. P. Palao and R. Kosloff, *Phys. Rev. A: At., Mol., Opt. Phys.*, 2003, **68**, 062308.
44 H. Rabitz, *Adv. Chem. Phys.*, 1997, **110**, 315 325.
45 C. P. Koch, J. P. Palao, R. Kosloff and F. Masnou Seeuws, *Phys. Rev. A: At., Mol., Opt. Phys.*, 2004, **70**, 013402.
46 J. P. Palao and R. Kosloff, *Phys. Rev. Lett.*, 2002, **89**, 188301.
47 U. Troppmann, C. Gollub and R. de Vivie Riedle, *New J. Phys.*, 2006, **8**, 100.
48 D. Geppert and R. de Vivie Riedle, *Chem. Phys. Lett.*, 2005, **404**, 289 295.
49 R. de Vivie Riedle, K. Sundermann and M. Motzkus, *Faraday Discuss.*, 1999, **113**, 0 15.
50 C. Gollub, M. Kowalewski and R. de Vivie Riedle, *Phys. Rev. Lett.*, 2008, **101**, 073002.
51 C. Gollub, M. Kowalewski, S. Thallmair and R. de Vivie Riedle, *Phys. Chem. Chem. Phys.*, 2010, **12**, 15780 15787.
52 A. V. Oppenheimer, R. W. Schaffer and J. Buck, *Discrete Time Signal Processing*, Prentice Hall, Upper Saddle River, NJ, 1999.
53 M. Lapert, R. Tehini, G. Turinici and D. Sugny, *Phys. Rev. A: At., Mol., Opt. Phys.*, 2009, **79**, 063411.
54 K. Kormann, S. Holmgren and H. O. Karlsson, *J. Optim. Theory Appl.*, 2010, **147**, 491 506.
55 *Molecular Switches*, ed. B. L. Feringa, Wiley VCH Verlag GmbH, 2001.
56 I. B. Ramsteiner, A. Hartschuh and H. Port, *Chem. Phys. Lett.*, 2001, **343**, 83 90.
57 J. M. Endtner, F. Effenberger, A. Hartschuh and H. Port, *J. Am. Chem. Soc.*, 2000, **122**, 3037 3046.
58 P. J. Reid, S. J. Doig, S. D. Wickham and R. A. Mathies, *J. Am. Chem. Soc.*, 1993, **115**, 4754 4763.
59 M. O. Trulson, G. D. Dollinger and R. A. Mathies, *J. Chem. Phys.*, 1989, **90**, 4274 4281.
60 S. Lochbrunner, W. Fuß, W. E. Schmid and K. L. Kompa, *J. Phys. Chem. A*, 1998, **102**, 9334 9344.
61 S. H. Pullen, N. A. Anderson, L. A. Walker II. and R. J. Sension, *J. Chem. Phys.*, 1998, **108**, 556 563.
62 P. Celani, F. Bernardi, M. A. Robb and M. Olivucci, *J. Phys. Chem.*, 1996, **100**, 19364 19366.
63 P. Celani, S. Ottani, M. Olivucci, F. Bernardi and M. A. Robb, *J. Am. Chem. Soc.*, 1994, **116**, 10141 10151.
64 M. Garavelli, P. Celani, M. Fato, M. J. Bearpark, B. R. Smith, M. Olivucci and M. A. Robb, *J. Phys. Chem. A*, 1997, **101**, 2023 2032.
65 A. Hofmann and R. de Vivie Riedle, *J. Chem. Phys.*, 2000, **112**, 5054 5059.
66 A. Hofmann and R. de Vivie Riedle, *Chem. Phys. Lett.*, 2001, **346**, 299 304.
67 D. Geppert, L. Seyfarth and R. de Vivie Riedle, *Appl. Phys. B: Lasers Opt.*, 2004, **79**, 987 992.
68 D. Geppert and R. de Vivie Riedle, *J. Photochem. Photobiol., A*, 2006, **180**, 282 288.
69 D. Geppert, A. Hofmann and R. de Vivie Riedle, *J. Chem. Phys.*, 2003, **119**, 5901 5906.
70 T. Brixner and G. Gerber, *ChemPhysChem.*, 2003, **4**, 418 438.
71 F. Krausz and M. Y. Ivanov, *Rev. Mod. Phys.*, 2009, **81**, 163.
72 M. F. Kling, C. Siedschlag, A. J. Verhoef, J. I. Khan, M. Schultze, T. Uphues, Y. Ni, M. Uiberacker, M. Drescher, F. Krausz and M. J. J. Vrakking, *Science*, 2006, **312**, 246 248.
73 B. J. Sussman, D. Townsend, M. Y. Ivanov and A. Stolow, *Science*, 2006, **314**, 278 281.
74 E. T. Sleva, J. I. M. Xavier and A. H. Zewail, *J. Opt. Soc. Am. B*, 1986, **3**, 483 487.
75 S. R. Hartmann and E. L. Hahn, *Phys. Rev.*, 1962, **128**, 2042 2053.
76 A. D. Hammerich, R. Kosloff and D. Tannor, *Phys. Rev. Lett.*, 1992, **69**, 2172.
77 M. Wollenhaupt, A. Prakelt, C. Sarpe Tudoran, D. Liese and T. Baumert, *J. Opt. B: Quantum Semiclassical Opt.*, 2005, **7**, S270.
78 M. Wollenhaupt, A. Prakelt, C. Sarpe Tudoran, D. Liese and T. Baumert, *J. Mod. Opt.*, 2005, **52**, 2187 2195.
79 M. Wollenhaupt, D. Liese, A. Prakelt, C. Sarpe Tudoran and T. Baumert, *Chem. Phys. Lett.*, 2006, **419**, 184 190.
80 M. Wollenhaupt, A. Prakelt, C. Sarpe Tudoran, D. Liese and T. Baumert, *Appl. Phys. B: Lasers Opt.*, 2006, **82**, 183 188.
81 P. von den Hoff, M. Kowalewski and R. de Vivie Riedle, *Faraday Discuss*, 2011, **153**, 159 171.
82 H. J. Werner, P. J. Knowles, R. Lindh, F. R. Manby, M. Schutz, P. Celani, T. Korona, G. Rauhut, R. D. Amos, A. Bernhardsson, A. Berning, D. L. Cooper, M. J. O. Deegan, A. J. Dobbyn, F. Eckert, C. Hampel, G. Hetzer, A. W. Lloyd, S. J. McNicholas, W. Meyer, M. E. Mura, A. Nicklass, P. Palmieri, R. Pitzer, U. Schumann, H. Stoll, A. J. Stone, R. Tarroni and T. Thorsteinsson, *MOLPRO, version 2006.1, a package of ab initio programs*, 2006, see http://www.molpro.net.
83 S. Magnier and P. Millié, *Phys. Rev. A: At., Mol., Opt. Phys.*, 1996, **54**, 204 218.
84 P. Fuentealba, H. Preuss, H. Stoll and L. v. Szentpaly, *Chem. Phys. Lett.*, 1982, **89**, 418.
85 W. Muller and W. Meyer, *J. Chem. Phys.*, 1984, **80**, 3311.
86 G. H. Jeung, *J. Mol. Spectrosc.*, 1997, **182**, 113 117.
87 P. von den Hoff, R. Siemering, M. Kowalewski and R. de Vivie Riedle, *IEEE J. Sel. Top. Quantum Electron.*, 2012, **18**, 119 129.
88 H. Rabitz, *J. Mod. Opt.*, 2004, **51**, 2469 2475.
89 M. Brune, F. Schmidt Kaler, A. Maali, J. Dreyer, E. Hagley, J. M. Raimond and S. Haroche, *Phys. Rev. Lett.*, 1996, **76**, 1800 1803.
90 F. Schmidt Kaler, H. Haffner, M. Riebe, S. Gulde, G. P. T. Lancaster, T. Deuschle, C. Becher, C. F. Roos, J. Eschner and R. Blatt, *Nature*, 2003, **422**, 408 411.
91 D. Leibfried, E. Knill, S. Seidelin, J. Britton, R. B. Blakestad, J. Chiaverini, D. B. Hume, W. M. Itano, J. D. Jost, C. Langer, R. Ozeri, R. Reichle and D. J. Wineland, *Nature*, 2005, **438**, 639 642.
92 J. A. Jones and M. Mosca, *J. Chem. Phys.*, 1998, **109**, 1648 1653.
93 R. Marx, A. F. Fahmy, J. M. Myers, W. Bermel and S. J. Glaser, *Phys. Rev. A: At., Mol., Opt. Phys.*, 2000, **62**, 012310.
94 P. Nuernberger, G. Vogt, T. Brixner and G. Gerber, *Phys. Chem. Chem. Phys.*, 2007, **9**, 2470.
95 C. M. Tesch, L. Kurtz and R. de Vivie Riedle, *Chem. Phys. Lett.*, 2001, **343**, 633.
96 R. de Vivie Riedle and U. Troppmann, *Chem. Rev.*, 2007, **107**, 5082 5100.
97 J. Vala, Z. Amitay, B. Zhang, S. R. Leone and R. Kosloff, *Phys. Rev. A: At., Mol., Opt. Phys.*, 2002, **66**, 062316.

98 R. Zadoyan, D. Kohen, D. A. Lidar and V. A. Apkarian, *Chem. Phys.*, 2001, **266**, 323.
99 Z. Bihary, D. R. Glenn, D. A. Lidar and V. A. Apkarian, *Chem. Phys. Lett.*, 2002, **360**, 459.
100 Y. Ohtsuki, *Chem. Phys. Lett.*, 2005, **404**, 126 131.
101 C. M. Tesch and R. de Vivie Riedle, *J. Chem. Phys.*, 2004, **121**, 12158 12168.
102 B. M. R. Korff, U. Troppmann and R. de Vivie Riedle, *J. Chem. Phys.*, 2005, **123**, 244509.
103 T. Witte, J. S. Yeston, M. Motzkus, E. J. Heilweil and K. L. Kompa, *Chem. Phys. Lett.*, 2004, **392**, 156 161.
104 D. B. Strasfeld, S. H. Shim and M. T. Zanni, *Phys. Rev. Lett.*, 2007, **99**, 038102.
105 M. J. Frisch, G. W. Trucks, H. B. Schlegel, G. E. Scuseria, M. A. Robb, J. R. Cheeseman, J. A. Montgomery Jr, T. Vreven, K. N. Kudin, J. C. Burant, J. M. Millam, S. S. Iyengar, J. Tomasi, V. Barone, B. Mennucci, M. Cossi, G. Scalmani, N. Rega, G. A. Petersson, H. Nakatsuji, M. Hada, M. Ehara, K. Toyota, R. Fukuda, J. Hasegawa, M. Ishida, T. Nakajima, Y. Honda, O. Kitao, H. Nakai, M. Klene, X. Li, J. E. Knox, H. P. Hratchian, J. B. Cross, C. Adamo, J. Jaramillo, R. Gomperts, R. E. Stratmann, O. Yazyev, A. J. Austin, R. Cammi, C. Pomelli, J. W. Ochterski, P. Y. Ayala, K. Morokuma, G. A. Voth, P. Salvador, J. J. Dannenberg, V. G. Zakrzewski, S. Dapprich, A. D. Daniels, M. C. Strain, O. Farkas, D. K. Malick, A. D. Rabuck, K. Raghavachari, J. B. Foresman, J. V. Ortiz, Q. Cui, A. G. Baboul, S. Clifford, J. Cioslowski, B. B. Stefanov, G. Liu, A. Liashenko, P. Piskorz, I. Komaromi, R. L. Martin, D. J. Fox, T. Keith, M. A. Al Laham, C. Y. Peng, A. Nanayakkara, M. Challacombe, P. M. W. Gill, B. Johnson, W. Chen, M. W. Wong, C. Gonzalez and J. A. Pople, *Gaussian 03, Revision D.01*, Gaussian, Inc, Pittsburgh PA, 2003.
106 R. Kosloff and H. Tal Ezer, *Chem. Phys. Lett.*, 1989, **127**, 223.
107 M. Tsubouchi and T. Momose, *J. Opt. Soc. Am. B*, 2007, **24**, 1886 1900.
108 N. Belabas, J. P. Likforman, L. Canioni, B. Bousquet and M. Joffre, *Opt. Lett.*, 2001, **26**, 743 745.
109 F. Eickemeyer, R. A. Kaindl, M. Woerner, T. Elsaesser and A. M. Weiner, *Opt. Lett.*, 2000, **25**, 1472.
110 H. S. Tan and W. S. Warren, *Opt. Express*, 2003, **11**, 1021 1028.
111 T. Witte, D. Zeidler, D. Proch, K. L. Kompa and M. Motzkus, *Opt. Lett.*, 2002, **27**, 131.
112 S. H. Shim, D. B. Strasfeld, E. C. Fulmer and M. T. Zanni, *Opt. Lett.*, 2006, **31**, 838 840.
113 S. H. Shim, D. B. Strasfeld and M. T. Zanni, *Opt. Express*, 2006, **14**, 13120 13130.
114 GAlib genetic algorithm package: Matthew Wall, Massachusetts Institute of Technology.
115 T. Hornung, M. Motzkus and R. de Vivie Riedle, *J.. Chem. Phys.*, 2001, **115**, 3105 3111.
116 D. Weidinger and M. Gruebele, *Mol. Phys.*, 2007, **105**, 1999 2008.
117 M. Ndong, D. Lauvergnat, X. Chapuisat and M. Desouter Lecomte, *J. Chem. Phys.*, 2007, **126**, 244505.
118 M. Tsubouchi and T. Momose, *Phys. Rev. A: At., Mol., Opt. Phys.*, 2008, **77**, 052326.
119 B. Schneider, C. Gollub, K. Kompa and R. de Vivie Riedle, *Chem. Phys.*, 2007, **338**, 291.
120 E. Zitzler and L. Thiele, *IEEE Trans. Evol. Comput.*, 1999, **3**, 257.
121 K. Deb, A. Pratap, S. Agarwal and T. Meyarivan, *IEEE Trans. Evol. Comput.*, 2002, **6**, 182.
122 L. Bonacina, J. Extermann, A. Rondi, V. Boutou and J. P. Wolf, *Phys. Rev. A: At., Mol., Opt. Phys.*, 2007, **76**, 023408.
123 C. Gollub and R. de Vivie Riedle, *Phys. Rev. A: At., Mol., Opt. Phys.*, 2009, **79**, 021401(R).
124 M. Artamonov, T. S. Ho and H. Rabitz, *Chem. Phys.*, 2004, **305**, 213.
125 J. Werschnik and E. Gross, *J. Opt. B: Quantum Semiclassical Opt.*, 2005, **7**, S300.
126 H. Tal Ezer and R. Kosloff, *J. Chem. Phys.*, 1984, **81**, 3967.
127 K. Ando, K. N. Houk, J. Busch, A. Menassé and U. Séquin, *J. Org. Chem.*, 1998, **63**, 1761 1766.
128 S. Yamazaki and S. Yamabe, *J. Org. Chem.*, 2002, **67**, 9346 9353.
129 J. L. Ye, P. Q. Huang and X. Lu, *J. Org. Chem.*, 2007, **72**, 35 42.
130 M. Hentschel, R. Kienberger, C. Spielmann, G. A. Reider, N. Milosevic, T. Brabec, P. B. Corkum, U. Heinzmann, M. Drescher and F. Krausz, *Nature*, 2001, **414**, 509.
131 A. Baltuška, T. Udem, M. Uiberacker, M. Hentschel, E. Goulielmakis, C. Gohle, R. Holzwarth, V. S. Yakovlev, A. Scrinzi, T. W. Hansch and F. Krausz, *Nature*, 2003, **421**, 611.
132 P. Cattaneo and M. Persico, *J. Phys. Chem. A*, 1997, **101**, 3454 3460.
133 G. J. Atchity and K. Ruedenberg, *J. Chem. Phys.*, 1999, **110**, 4208 4212.
134 C. Leforestier, R. H. Bisseling, C. Cerjan, M. D. Feit, R. Friesner, A. Guldberg, A. Hammerich, G. Jolicard, W. Karrlein, H. D. Meyer, N. Lipkin, O. Roncero and R. Kosloff, *J. Comp. Physiol.*, 1991, **94**, 59 80.
135 A. Wirth, M. T. Hassan, I. Grguraš, J. Gagnon, A. Moulet, T. T. Luu, S. Pabst, R. Santra, Z. A. Alahmed, A. M. Azzeer, V. S. Yakovlev, V. Pervak, F. Krausz and E. Goulielmakis, *Science*, 2011, **334**, 195 200.